

# GeoFormer: A Swin Transformer-Based Framework for Scene-Level Building Height and Footprint Estimation from Sentinel Imagery

Jinzen Han<sup>1</sup>, JinByeong Lee<sup>1</sup>, JiSung Kim<sup>2</sup>, MinKyung Cho<sup>3</sup>,  
DaHee Kim<sup>3</sup>, and HongSik Yun<sup>1,\*</sup>

<sup>1</sup>Dept. of Civil, Architectural and Environmental System Engineering, Sungkyunkwan University, South Korea

<sup>2</sup>School of Geography, University of Leeds, United Kingdom

<sup>3</sup>Interdisciplinary Program for Crisis, Disaster and Risk Management, Sungkyunkwan University, South Korea

\*Corresponding author: [yoonhs@skku.edu](mailto:yoonhs@skku.edu)

## Abstract

Accurate three-dimensional urban data are critical for climate modelling, disaster risk assessment, and urban planning, yet remain scarce due to reliance on proprietary sensors or poor cross-city generalisation. We propose **GeoFormer**, an open-source Swin Transformer framework that jointly estimates building height (BH) and footprint (BF) on a 100 m grid using only Sentinel-1/2 imagery and open DEM data. A geo-blocked splitting strategy ensures strict spatial independence between training and test sets. Evaluated over 54 diverse cities, GeoFormer achieves a BH RMSE of 3.19 m and a BF RMSE of 0.05—improving 7.5 % and 15.3 % over the strongest CNN baseline—while maintaining < 3.5 m BH RMSE in cross-continent transfer. Ablation studies confirm that DEM is indispensable for height estimation and that optical reflectance dominates over SAR, though multi-source fusion yields the best overall accuracy. All code, weights, and global products are publicly released.

**Keywords:** Building footprint, Building height, Remote sensing, Sentinel, Urban 3-D mapping

## 1 Introduction

In recent decades, urban areas across the globe—especially in Asia—have undergone dramatic three-dimensional transformations driven by population growth, land scarcity, and vertical densification. Studies have documented not only horizontal expansion but also a shift toward vertical urban development, particularly in megacities such as Beijing and Seoul [8, 10, 11]. This transition has profound implications for urban climate, infrastructure, and risk management.

Building height (BH) and building footprint (BF) are critical indicators of urban form. Accurate BH and BF data are essential for modelling urban heat islands [36, 28], estimating flood exposure [15], and simulating cascading disasters such as fire-following-earthquakes [33]. However, despite their significance, public access to consistent and high-resolution 3D urban data remains limited—particularly in the Global South [12]. Even in data-rich regions such as South Korea, recent surveys show that only 30–40% of buildings include height attributes.

Numerous methods have been developed to estimate BH and BF, ranging from rule-based and empirical regression models [21, 3], to machine learning [9, 6] and deep learning approaches based on U-Net or SEResNet architectures [2, 22, 20]. A detailed comparison of representative studies is summarised in Table 1. These studies span a wide range of input data sources, spatial resolutions, and geographical scopes. While object-level methods using very-high-resolution (VHR) optical or LiDAR data often achieve the highest accuracies (e.g., RMSE < 2 m for BH at per-building scale), they are inherently limited in scalability due to the high cost, restricted coverage, and infrequent update cycles of the underlying datasets. Grid-based approaches using open-access Sentinel-1 SAR and Sentinel-2 MSI imagery have demonstrated much broader spatial coverage, but they often rely on auxiliary information—such as cadastral footprints, land-use maps, slope, or other thematic layers—during inference [35, 5]. This dependency constrains their applicability in regions where such auxiliary data are unavailable, outdated, or inconsistent, and also hinders direct global-scale deployment. In addition, traditional machine learning approaches typically require the manual design and selection of input features, which can limit their ability to capture complex spatial–spectral relationships and reduce adaptability when transferring to new regions or sensor types.

More recently, a new wave of studies has sought to overcome these constraints through advanced architectures and data-fusion strategies. Wang et al. [34] introduced MF-BHNet, a hybrid Transformer–CNN encoder that fuses Sentinel-1 and Sentinel-2 features with cross-modal attention at 10 m resolution. Zheng et al. [37] proposed NeCT-Net, which integrates spaceborne LiDAR with multisource remote sensing via a CNN–Transformer hybrid for individual building-height retrieval, yet its reliance on ICESat-2 point clouds limits spatial continuity. Mostafavi et al. [26] released UT-GLOBUS, providing per-building heights and urban canopy parameters for over 1 200 cities by combining ICESat-2 altimetry with machine learning; however, the method requires pre-existing building footprint inventories (e.g., from OpenStreetMap) as input, limiting its applicability where such vector data are incomplete or unavailable. At even finer scales, Zhu et al. [38] released the GlobalBuildingAtlas, mapping 2.75 billion buildings worldwide at 3 m resolution using PlanetScope imagery; however, this product relies on commercial satellite data rather than freely available Sentinel sensors. These advances—while impressive—underscore a persistent trade-off between spatial resolution, data dependency, and global accessibility.

As indicated in Table 1, many of the recent Sentinel-based models focus on either BH or BF alone, without explicitly leveraging the potential benefits of joint estimation, and few have been validated across multiple countries or markedly different urban morphologies.

Furthermore, several studies have highlighted the limitations of using 10 m spatial resolution for urban mapping tasks. For example, Schug et al. [32] demonstrated that even with advanced regression-based unmixing, Sentinel-1/2 data at 10 m resolution struggled to capture small and densely packed urban structures, leading to systematic underestimation of built-up areas. Similarly, Radoux et al. [30] reported that many fine-scale landscape

Table 1: Comparison of recent BH/BF estimation models with dataset and resolution

Paper (1st author, Year)	Method / Model	Dataset	Spatial res. *	Out. Accuracy	District
Park & Guldmann 2019	Random Forest (ML)	LiDAR	Per-bldg	BH OA 96.5 %	Local
Sun Y. <i>et al.</i> 2019	FCN (DL)	VHR SAR	Per-bldg	BH RMSE 3.51 m	Local
Milojevic-Dupont <i>et al.</i> 2020	RF/XGBoost (ML)	GIS only	Per-bldg	BH MAE 2.5 m	Local
Li X. <i>et al.</i> 2020	Empirical Regression	Sentinel + LiDAR	Per-bldg	BH RMSE 1.5 m	Local
Rapuzzi <i>et al.</i> 2020	CNN (DL)	Sentinel	Per-bldg	BF F1 0.75	Local
Li Z. <i>et al.</i> 2021	U-Net (DL)	VHR satellite image	Per-bldg	BH IoU 0.851	Local
Frantz <i>et al.</i> 2021	SVR (ML)	Sentinel	10 m grid	BH wRMSE 2.9–3.5 m	Local
Buyukdemircioglu <i>et al.</i> 2022	U-Net (DL)	VHR satellite image	Per-bldg	BF F1 97.31 %	Local
Rastogi <i>et al.</i> 2022	U-Net (DL)	VHR satellite image	Per-bldg	BF IoU 0.75	Local
Li R. <i>et al.</i> 2023	SEResNet (DL)	Sentinel	100 m grid	BH/BRMSE 5.26 m	Global
Wu <i>et al.</i> 2023	Random Forest (ML)	Sentinel	10 m grid	BH RMSE 6.1 m	Local
Cai B. <i>et al.</i> 2023	U-Net (DL)	Sentinel	10 m grid	BH RMSE 4.65 m	Local
Che <i>et al.</i> 2024	XGBoost (ML)	Sentinel + ALOS	Per-bldg	BH RMSE 1.9–14.6 m; $R^2$ 0.66–0.96	Global
Dabrock <i>et al.</i> 2024	XGBoost (ML)	Sentinel	Per-bldg	BH MAE 1.78 m	Local
Chen Y. <i>et al.</i> 2024	Random Forest (ML)	Sentinel	10 m grid	BF MAE 3.43–5.06 m	Local
Cai P. <i>et al.</i> 2024	Empirical Regression	Sentinel + LiDAR	Per-bldg	BH RMSE 8.1 m	Local
Wang <i>et al.</i> 2024	Transformer+CSN (DL)	Sentinel-1/2	10 m grid	BH RMSE ~3.5 m	Multi-country
Mostafavi <i>et al.</i> 2024	ML + ICESat-2 (ML)	ICESat-2 + Sentinel	Per-bldg	BH 1200+ cities	Global
Chen Yuehong <i>et al.</i> 2025	SBHE (CNN)	Sentinel	10 m grid	BH RMSE 4.62 m	Local
Yadav <i>et al.</i> 2025	T-SwinUNet (Transformer)	Sentinel-1/2 time series	10 m grid	BH RMSE 1.89 m	Europe (multi-country)
Zheng <i>et al.</i> 2025	NeCT-Net (CNN-Trans.)	LiDAR + Sentinel	Per-bldg	BH —	Local
Zhu <i>et al.</i> 2025	ML pipeline	PlanetScope	3 m / Per-bldg	BH/BF 75B buildings mapped	Global
<b>Ours (GeoFormer)</b>	<b>Swin Transformer</b>	<b>Sentinel + DEM</b>	<b>100 m grid</b>	<b>BH/BRMSE 3.19 m (BH)</b>	<b>Global</b>

*Note:* Spatial resolution is categorized as “Per-bldg” for object-level results or “Pixel/Grid” for fixed raster outputs.

features fall well below the spatial sampling unit of Sentinel-2, resulting in sub-pixel mixing and reduced classification accuracy. This limitation is particularly evident in cities such as Seoul, where local building regulations stipulate a minimum separation distance of 10 m between residential buildings to ensure privacy and safety during emergencies. In high-density urban areas, many buildings are positioned at or near this minimum spacing, causing multiple structures to fall within a single 10 m pixel. Such proximity leads to severe mixed-pixel effects, making it difficult to resolve individual buildings and accurately estimate BH and BF. These constraints motivate the adoption of aggregated grids (e.g., 100 m) combined with multi-source data integration for robust large-scale urban analysis.

An important consideration is whether finer-resolution models (e.g., 10 m) can simply be aggregated to produce 100 m outputs, thereby rendering direct 100 m modelling unnecessary. We argue that this view overlooks several critical factors. First, pixel-level models optimise per-pixel loss functions and are not trained to minimise scene-level aggregation error; systematic biases (e.g., underestimation of tall buildings) propagate and may even amplify upon spatial averaging. Second, finer-resolution approaches incur a computational overhead that is roughly  $10^4$  times greater for global coverage at 10 m than at 100 m, making routine updates prohibitively expensive for many institutions—especially in the Global South. Third, a model operating natively at 100 m can adopt a spatial-neighbourhood mechanism (e.g., GeoFormer’s  $5 \times 5 = 500$  m context window) that captures urban-block morphology in a physically meaningful and computationally tractable manner; achieving equivalent contextual coverage at 10 m would require processing  $50 \times 50$  pixel patches per token—a configuration that is neither practical nor commonly attempted. In short, while post-hoc aggregation of finer-resolution predictions is technically feasible, it is not optimised for the scene-level objective, imposes prohibitive computational costs at the global scale, and forgoes the contextual modelling advantages that a native 100 m framework can provide.

Moreover, numerous large-scale urban studies adopt spatial resolutions of 100 m or coarser to characterise city-scale morphology and related environmental parameters. For instance, Demuzere et al. [7] produced a global Local Climate Zone (LCZ) map to support Earth system modelling, while Qi et al. [29] generated a long-term LCZ dataset for the continental United States. Similarly, Kwok et al. [18] developed a refined urban dataset for Hong Kong to better represent its complex morphology in mesoscale climate models, and Bechtel et al. [1] demonstrated downscaling of urban land surface temperature in Hamburg, Germany. These examples indicate that providing building footprint and height at a 100 m resolution is highly valuable, as it aligns with the spatial scale commonly employed in city- and continental-scale analyses.

Considering the above factors—the limitations of 10 m resolution for densely built urban areas, the proven applicability of 100 m products in many large-scale studies, and the shortcomings of existing models—we propose **GeoFormer**, a Swin Transformer-based multi-task learning framework for joint building height (BH) and footprint (BF) prediction at 100 m resolution. GeoFormer relies solely on globally accessible Sentinel-1 SAR, Sentinel-2 MSI, and digital elevation model (DEM) data, avoiding any proprietary VHR imagery or vector sources. As shown in Figure 1, BH/BF reference labels are spatially aligned with satellite and DEM inputs on a unified 100 m grid, and a spatial partitioning strategy (GeoSplit) ensures strict independence between training and test regions. The Swin Transformer backbone, with configurable context windows ( $3 \times 3$ ,  $5 \times 5$ ,  $9 \times 9$ ), enables joint BH and BF estimation via multi-task learning.

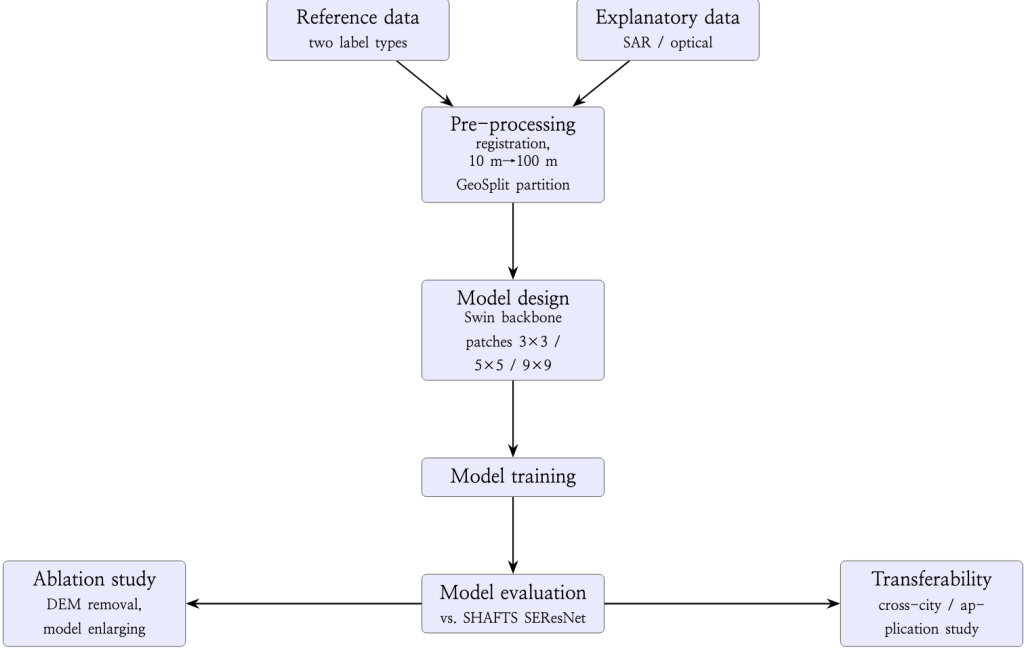


Figure 1: Workflow of the proposed GeoFormer framework.

When benchmarked against three representative single-patch CNN architectures—ResNet-MTL, UNet-MTL, and SENet-MTL—which are restricted to the target 100 m cell alone, GeoFormer with a  $5 \times 5$  neighbourhood achieves a BH RMSE of 3.19 m and a BF RMSE of 0.050, improving upon the strongest baseline (UNet) by 7.5 % and 15.3 %, respectively. Cross-city, cross-continent, and post-disaster evaluations confirm robust generalisation.

Ablation studies reveal three key findings: (i) excessive model capacity induces overfitting rather than improved generalisation; (ii) removing DEM substantially degrades BH accuracy while leaving BF largely unaffected, confirming the indispensable role of topographic context; and (iii) modality ablation shows that removing the optical channel causes far greater performance loss than removing SAR, indicating that multispectral reflectance is the primary driver for height retrieval at 100 m resolution—yet the full SAR+optical+DEM configuration remains optimal, validating the complementary value of multi-source fusion.

## 2 Data Preprocessing

### 2.1 Reference Data

This study adopts the open-source SHAFTS Reference Dataset (v2022.3) [20], which provides per-city building footprint and height metrics that have already been processed using Fishnet Analysis [27]. Specifically, a regular  $100 \text{ m} \times 100 \text{ m}$  grid was applied to vector building inventories by the SHAFTS authors to compute standardized spatial indices. These precomputed grid-based metrics are directly used in this study as reference labels.

As shown in Figure 2, Fishnet Analysis discretizes the urban space by overlaying a uniform grid on building polygons. Within each cell, the intersected building areas and their corresponding heights are used to derive cell-level statistics. This allows consistent



Figure 2: Illustration of Fishnet Analysis: a 100 m grid overlays vector building footprints to compute per-cell height and footprint coverage.

aggregation of spatial information and enables raster-format learning targets.

The two core indices, building footprint ratio and average building height, are defined as follows:

$$\lambda_p = \frac{\sum_{i \in \mathcal{J}} A_i}{(100 \text{ m})^2}, \quad (1)$$

$$H_{\text{ave}} = \frac{\sum_{i \in \mathcal{J}} A_i h_i}{\sum_{i \in \mathcal{J}} A_i}, \quad (2)$$

where  $\mathcal{J}$  denotes the set of buildings that spatially intersect a given 100 m grid cell,  $A_i$  is the intersection area between the  $i$ th building and the cell, and  $h_i$  is the height of the  $i$ th building. The footprint index  $\lambda_p$  measures the proportion of the cell covered by building structures, while the average building height  $H_{\text{ave}}$  is computed as the area-weighted mean of building heights within the cell. Note that both metrics are normalized within the fixed 100 m  $\times$  100 m spatial unit, enabling consistent comparisons across diverse urban morphologies.

As shown in Figure 3, this study uses a total of 51 cities from the SHAFTS dataset that explicitly provide building height attributes. These cities are geographically diverse, cov-

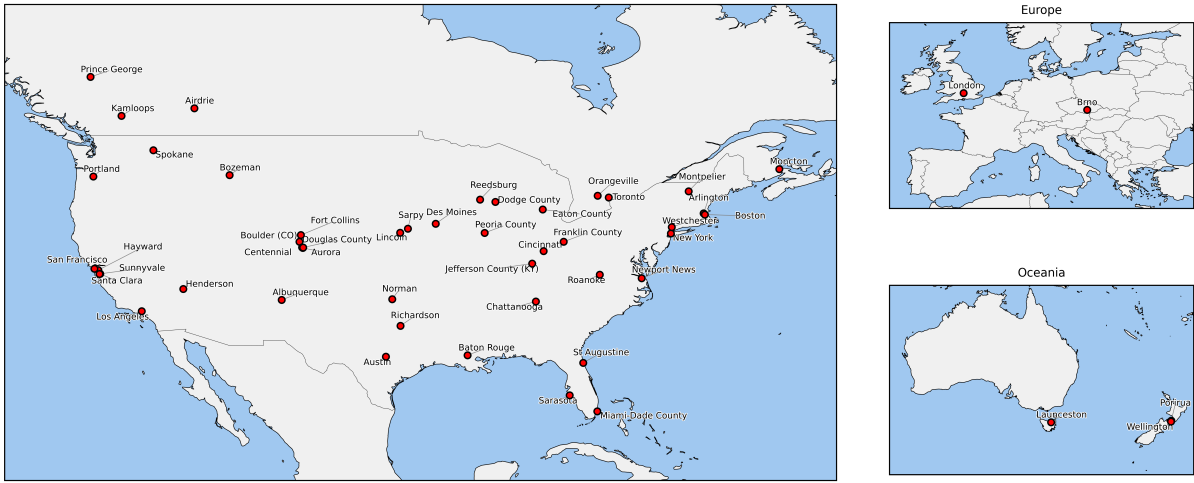


Figure 3: Geographic distribution of SHAFTS (v2022.3) reference cities.

Table 2: Explanatory Data Sources and Specifications

Data Source	Specification
Sentinel-1 GRD Level-1	10 m VV and VH polarizations
Sentinel-2 Level-2A	10 m red, green, blue, and near-infrared (B2, B3, B4, B8)
SRTM V3 DEM	30 m digital elevation model

ering multiple continents and urban morphologies, and thus offer a broad representation of global built environments for robust model training and evaluation.

## 2.2 Explanatory Data and Processing

This study employs three open geospatial sources as explanatory variables: Sentinel-1 Synthetic Aperture Radar (SAR), Sentinel-2 multispectral optical imagery, and Shuttle Radar Topography Mission (SRTM) digital elevation data. The corresponding specifications are summarized in Table 2. Sentinel imagery was processed at 10 m resolution, while SRTM DEM was used at 30 m resolution.

SAR backscatter captures surface characteristics via three scattering mechanisms: surface scattering (weak and specular), volume scattering (diffuse return from volumetric targets), and double-bounce scattering (strong signal from vertical structures). Optical reflectance reveals material-specific spectral signatures and surface textures, useful for distinguishing man-made structures. SRTM DEM provides global elevation priors essential for terrain-aware modeling.

To acquire these datasets, we implemented an automated download pipeline on the Google Earth Engine (GEE) platform using JavaScript. For each city, the raster filename from the SHAFTS dataset was parsed to extract its geographic bounding box and acquisition year. These parameters were then used to retrieve Sentinel-1, Sentinel-2, and SRTM imagery. During the download process, additional preprocessing steps were applied, including cloud filtering (for Sentinel-2), annual percentile aggregation, and clipping to the padded city extent. This ensured that the explanatory data were temporally consistent,

cloud-free, and spatially aligned across all cities.

To construct a unified dataset suitable for model training and testing, the reference variables (i.e., building height and footprint) were combined with the corresponding explanatory variables (i.e., Sentinel and DEM patches) on a per-sample basis. Prior to this integration, a set of filtering rules was applied to remove implausible or uninformative samples.

Each  $10 \times 10$  pixel patch corresponds to a 100 m grid cell. Implausible samples were removed based on three rules:

1.  $2.0 \leq H_{\text{ave}} \leq 500.0$  (m),
2.  $\lambda_p > 0.01$ ,
3. If  $\lambda_p < 0.04$ , then require  $H_{\text{ave}} < 20$  to exclude slivers.

These criteria ensure that (i) height values lie within a physically plausible range, (ii) the minimum detectable footprint reflects one-pixel coverage, and (iii) narrow artifacts with unrealistically high structures are excluded.

Filtered samples were consolidated into a unified HDF5 file, with each city stored as an individual group. Figure 4 illustrates the internal structure of one such group. Each group contains two types of reference labels (building height and footprint), multi-source explanatory variables (Sentinel-1, Sentinel-2, and DEM), and a pair of coordinate indices.

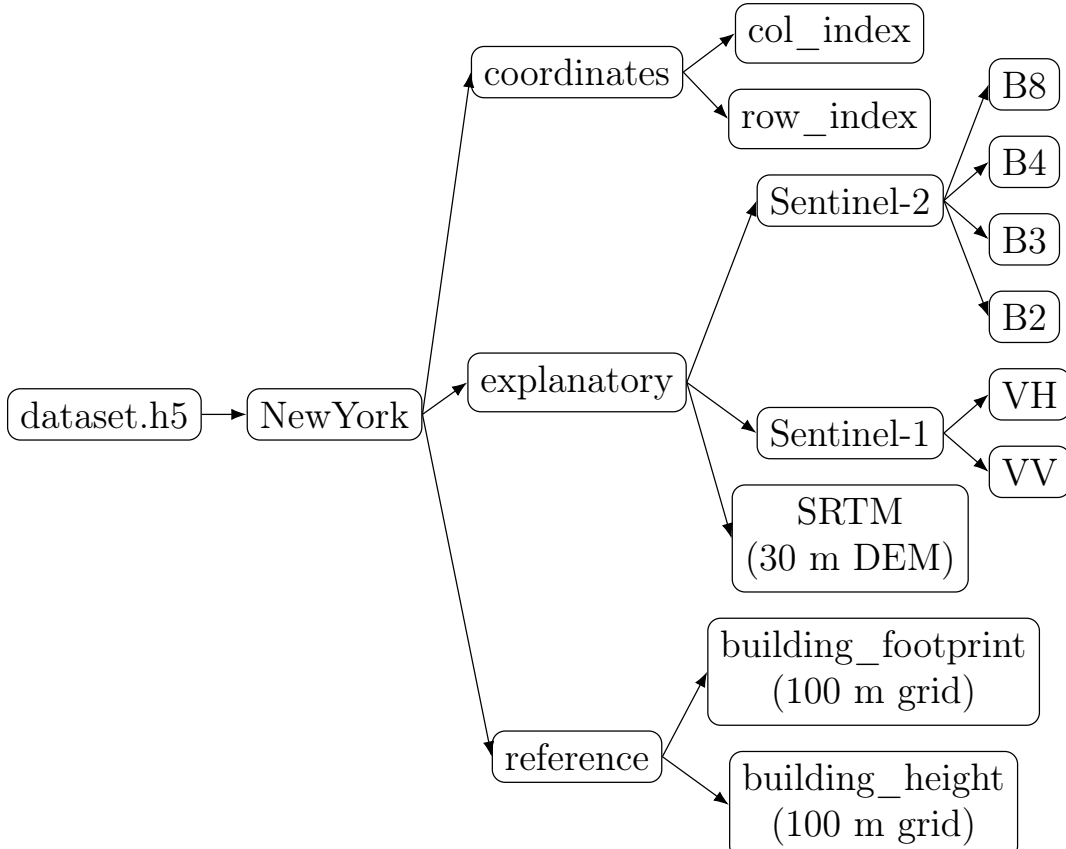


Figure 4: Structure of a single city group in the final HDF5 file.

The added `row_index` and `col_index` fields represent the grid-based location of each patch within the city, expressed in row–column units. These coordinates were appended after filtering to facilitate spatial operations such as neighborhood-aware patch concatenation during training.

In this study, the dataset is split into training, validation, and test sets using an 8:1:1 ratio. Unlike prior work that relies on fully random sampling, we address key limitations of such approaches, especially in the context of receptive-field-based modeling.

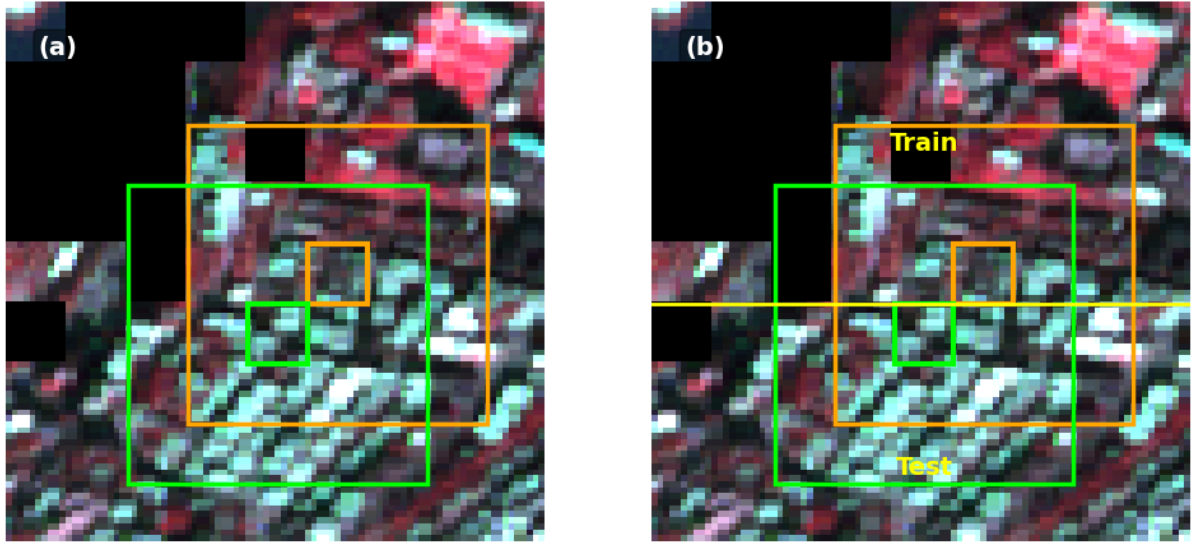


Figure 5: Data leakage from random sampling under dynamic receptive field concatenation.

As shown in Figure 5, random partitioning can lead to overlap between training and test patches when dynamic context concatenation is applied at runtime. This overlap may cause the model to unintentionally observe parts of the test region during training, leading to performance inflation.

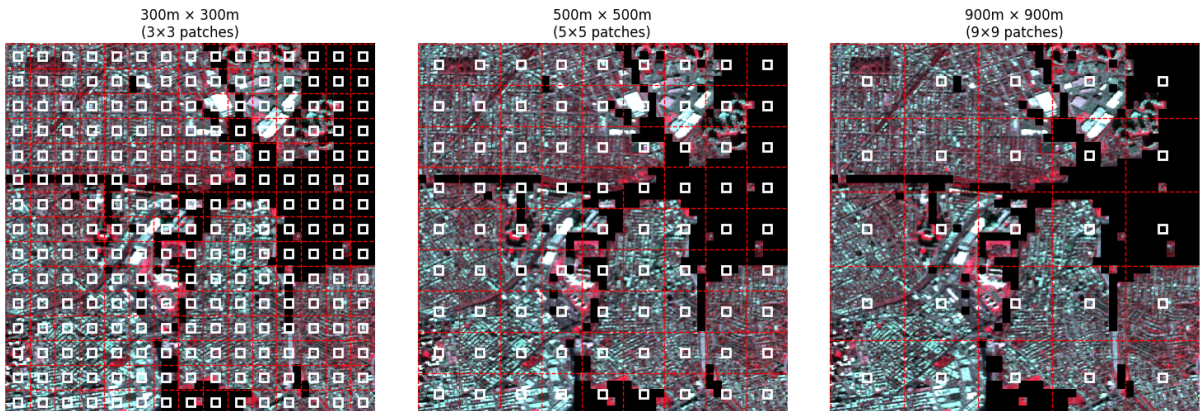


Figure 6: Sample reduction under static receptive field expansion.

Precomputing context patches in advance can eliminate such leakage. However, as shown in Figure 6, increasing the receptive field (e.g., from 100 m to 900 m) drastically reduces the number of usable samples, making fair cross-scale comparison difficult.

To overcome these issues, we adopt a spatially aware partitioning strategy based on the geographic layout of each city. Instead of random selection, each city is divided into ten equal-angle radial sectors centered on the urban core. These sectors are then allocated to the training, validation, and test sets using a greedy balancing strategy to approximate the desired 8:1:1 split while ensuring each subset contains both central and peripheral regions.

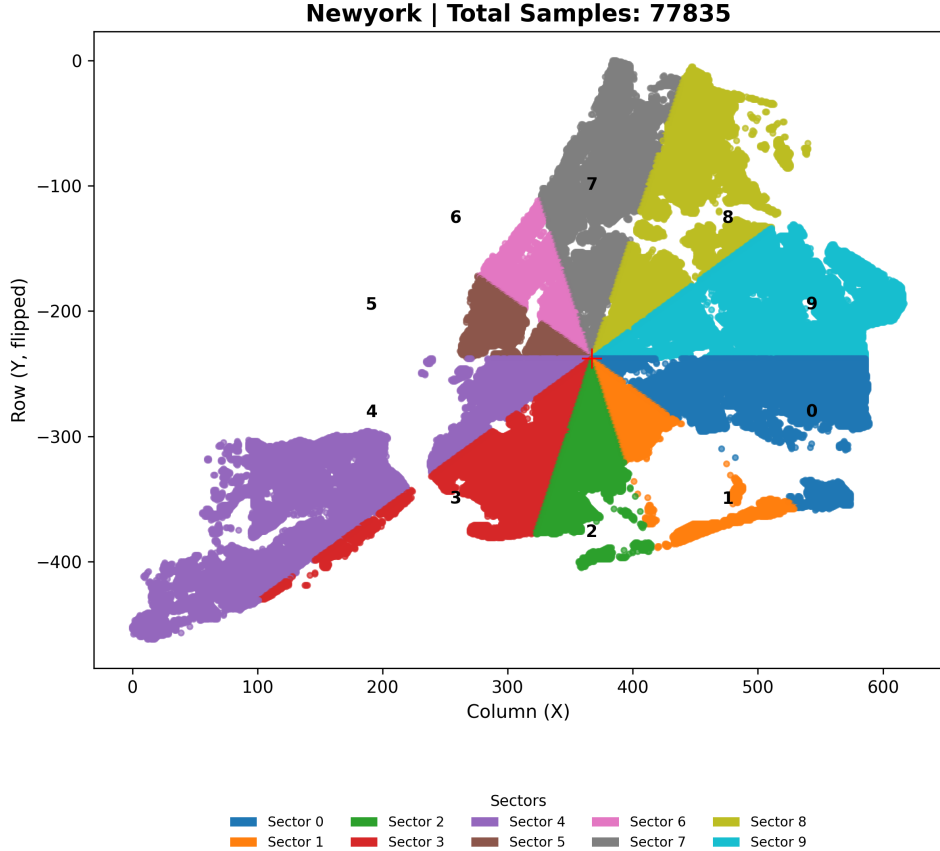


Figure 7: Radial sector division of New York City used for spatially balanced dataset partitioning.

Figure 7 illustrates the radial-sector partitioning for New York City. This strategy preserves spatial coherence within each subset and avoids training-test overlap along receptive field boundaries.

To verify the necessity of spatial partitioning, Figure 8 presents hexbin visualizations of building height (BH) and footprint (BF) relative to city centers. Both metrics show a clear decline from core to periphery, confirming the spatial heterogeneity of urban form.

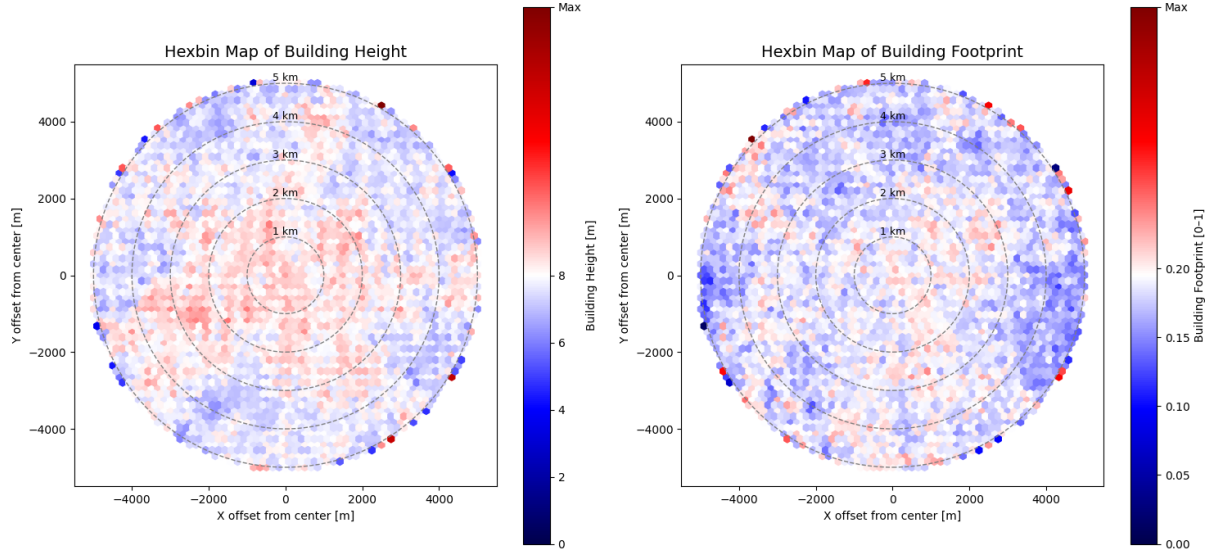


Figure 8: Hexbin-mapped distribution of building height and footprint across training cities.

Table 3: Ring-based statistics of building height and footprint

Radial Range (m)	Height Mean	Height Std.	Footprint Mean	Footprint Std.
0–1000	10.13	11.03	0.203	0.132
1000–2000	9.58	7.85	0.200	0.130
2000–3000	9.05	6.75	0.195	0.122
3000–4000	8.64	6.65	0.190	0.124
4000–5000	8.43	6.68	0.188	0.126

Table 3 further quantifies these gradients using concentric 1 km bands, showing consistent decreases in BH and BF with radial distance. This validates the need for spatially stratified sampling to maintain generalization under urban heterogeneity.

## 3 Methodology

### 3.1 Model Architecture

To estimate both building height (BH) and building footprint (BF) simultaneously, we design a Swin Transformer-based multi-task regression framework named **GeoFormer**. The complete architecture is depicted in Figure 9, which shows the flow of information from input preparation to final predictions.

GeoFormer processes fused multi-source remote sensing data—namely Sentinel-1 (SAR), Sentinel-2 (optical), and DEM—into a unified 8-band multi-channel tensor (see Figure 10). An additional binary mask channel is included to indicate valid (non-padded) regions, enabling the model to distinguish between central and contextual patches during both training and inference. This mask serves as a spatial prior that guides attention and loss computation toward valid areas, particularly when using dynamically constructed context

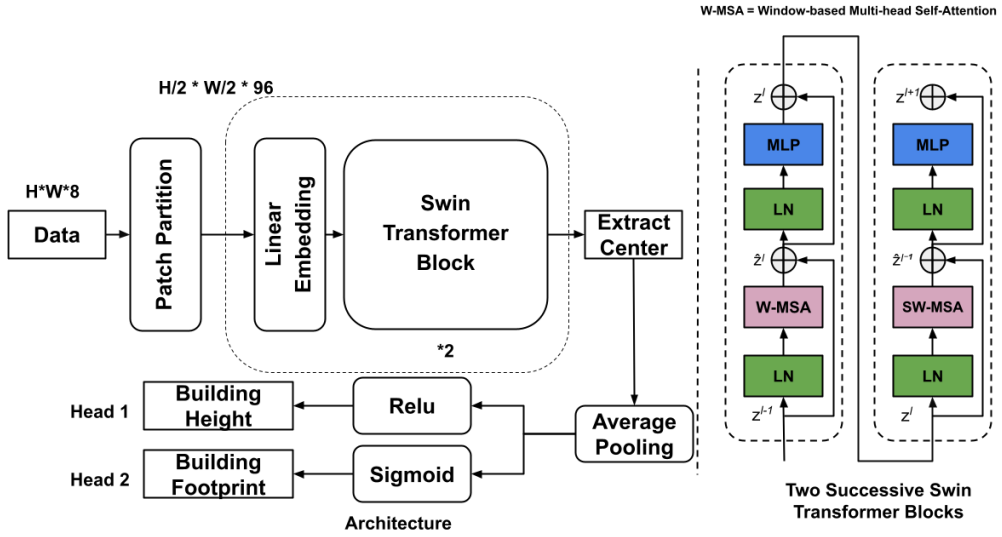


Figure 9: Architecture of GeoFormer: a Swin-based multi-task model for predicting building height and footprint.

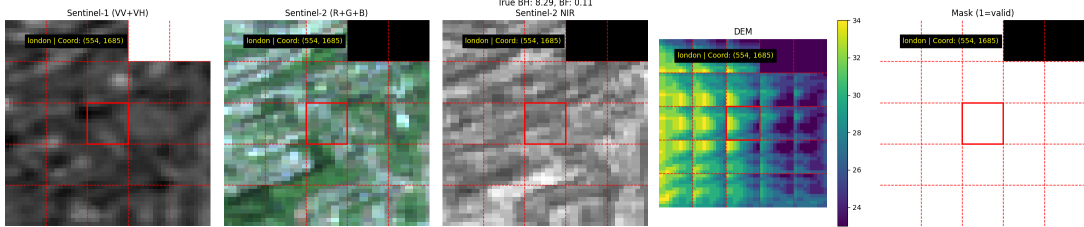


Figure 10: Illustration of the 8-band multi-source input tensor. From left to right: Sentinel-1 (VV, VH), Sentinel-2 (RGB+NIR), true BH, DEM, and the binary mask indicating the valid region (center patch).

windows.

The input tensor is then divided into fixed-size non-overlapping patches (e.g.,  $3 \times 3$ ,  $5 \times 5$ , or  $9 \times 9$  context windows), and each patch is linearly embedded into a token sequence as in the original Swin Transformer [23].

The token sequence passes through two successive Swin Transformer blocks, each consisting of alternating window-based multi-head self-attention (W-MSA) and shifted window attention (SW-MSA) modules, layer normalization (LN), and feedforward multilayer perceptrons (MLPs). This design allows GeoFormer to capture both local and global spatial dependencies efficiently.

After the backbone processing, we apply an **extract-center** module to isolate the representation of the central patch from the surrounding context. This center token—representing the target 100 m grid—is then passed through an average pooling layer and fed into two independent prediction heads.

Each head is a lightweight MLP tailored to one of the two tasks:

- The BH head uses a ReLU activation to regress building height.

- The BF head uses a sigmoid activation to constrain the footprint ratio between 0 and 1.

This architecture provides spatially aligned multi-task outputs, ensures computational efficiency via hierarchical feature reuse, and allows flexible control over the receptive field size through the patch grid configuration.

### 3.2 Loss Function

To jointly predict building height ( $y^{\text{bh}}$ ) and building footprint ratio ( $y^{\text{bf}}$ ), this study employs a multi-task loss function composed of two regression objectives. Following uncertainty-based weighting [17], the total loss is defined as:

$$\mathcal{L}_{\text{total}} = \frac{1}{2\sigma_{\text{bh}}^2} \mathcal{L}_{\text{bh}} + \frac{1}{2\sigma_{\text{bf}}^2} \mathcal{L}_{\text{bf}} + \log \sigma_{\text{bh}} + \log \sigma_{\text{bf}} \quad (3)$$

Here,  $\mathcal{L}_{\text{bh}}$  and  $\mathcal{L}_{\text{bf}}$  are regression losses for building height and footprint respectively, and  $\sigma_{\text{bh}}$ ,  $\sigma_{\text{bf}}$  are learnable task uncertainties optimized during training.

For each task, the Adaptive Huber Loss [16] is used, which combines the sensitivity of Mean Squared Error (MSE) with the robustness of Mean Absolute Error (MAE). It is defined as:

$$\text{HuberLoss}(\hat{y}, y) = \begin{cases} \frac{1}{2\delta}(\hat{y} - y)^2, & \text{if } |\hat{y} - y| < \delta \\ |\hat{y} - y| - \frac{\delta}{2}, & \text{otherwise} \end{cases} \quad (4)$$

Here,  $\hat{y}$  is the predicted value,  $y$  is the ground-truth, and  $\delta$  controls the transition between the quadratic and linear regimes. When residuals are small, the loss behaves like MSE; for large residuals, it behaves like MAE to mitigate the influence of outliers.

At the beginning of training,  $\delta$  is initialized based on the Mean Absolute Error (MAE) over the training set:

$$\delta^{(0)} = \frac{1}{N} \sum_{j=1}^N |\hat{y}_j - y_j| \quad (5)$$

During training,  $\delta$  is updated at each epoch using the residual statistics of the current model, allowing the loss function to dynamically adapt to prediction uncertainty.

This hybrid and adaptive design ensures both robustness and precision in geospatial regression tasks, making it well-suited for predicting building properties from satellite imagery.

### 3.3 Optimization and Training Settings

The model is trained using the AdamW optimizer [25], with an initial learning rate of  $1 \times 10^{-4}$  and a weight decay of  $1 \times 10^{-2}$ . To stabilize early-stage training and encourage smooth convergence, we adopt a cosine annealing learning rate schedule with warmup [24].

Mixed-precision training is enabled using automatic mixed precision (AMP) to accelerate convergence and reduce GPU memory usage. Early stopping and checkpointing are implemented based on validation  $R^2$  to ensure optimal generalization.

All experiments are conducted with a batch size of 64 and trained for up to 150 epochs or until convergence.

## 4 Model Evaluation

### 4.1 Evaluation Metrics and Justification

Table 4: Evaluation metrics used for regression accuracy assessment

Metric	Formula	Range	Direction	Focus
RMSE	$\sqrt{\frac{1}{N} \sum_{i=1}^N (\hat{y}_i - y_i)^2}$	$[0, \infty)$	Lower	Sensitive to outliers
MAE	$\frac{1}{N} \sum_{i=1}^N  \hat{y}_i - y_i $	$[0, \infty)$	Lower	Average error magnitude
ME	$\frac{1}{N} \sum_{i=1}^N (\hat{y}_i - y_i)$	$(-\infty, \infty)$	Close to 0	Overall bias / signed error
NMAD	$1.4826 \times \frac{\text{median}( \hat{y}_i - y_i - \text{median}(\hat{y}_i - y_i) )}{\text{median}( \hat{y}_i - y_i - \text{median}(\hat{y}_i - y_i) )}$	$[0, \infty)$	Lower	Robust to outliers
CC	$\frac{\text{Cov}(\hat{y}, y)}{\sigma_{\hat{y}} \sigma_y}$	$[-1, 1]$	Close to 1	Linear correlation
$R^2$	$1 - \frac{\sum_{i=1}^N (\hat{y}_i - y_i)^2}{\sum_{i=1}^N (y_i - \bar{y})^2}$	$(-\infty, 1]$	Close to 1	Variance explained by model

Table 4 summarizes the set of regression metrics employed in this study to evaluate the predictive performance of building height and footprint estimation. These metrics are carefully selected to provide a multi-perspective assessment, covering magnitude-based errors (RMSE, MAE), bias (ME), robustness to outliers (NMAD), and statistical correlation with ground-truth labels (CC and  $R^2$ ).

Root Mean Squared Error (RMSE) penalizes large residuals more heavily, making it sensitive to outliers, while Mean Absolute Error (MAE) captures the average prediction error in a more balanced manner. Mean Error (ME) provides a signed indication of systematic bias in predictions. The Normalized Median Absolute Deviation (NMAD) is particularly suited for datasets with non-Gaussian error distributions, offering a robust alternative to RMSE. Pearson’s Correlation Coefficient (CC) and the Coefficient of Determination ( $R^2$ ) jointly evaluate the consistency and explanatory power of the model outputs relative to the reference values.

Together, these metrics allow for a comprehensive evaluation of both overall model accuracy and stability under heterogeneous spatial conditions.

## 4.2 CNN Baseline Comparison

Before evaluating GeoFormer, we first benchmark three representative CNN architectures as single-patch baselines. Each model receives a single  $10 \times 10$  pixel patch (corresponding to one 100 m grid cell) and outputs joint BH and BF predictions through a shared backbone with two task-specific heads. All baselines adopt the same multi-task Huber loss and uncertainty-based weighting described in Section III-B, and are trained under identical data splits, augmentation, and optimization settings. The three architectures are:

- **ResNet-MTL** [13]: a residual network with skip connections that alleviate vanishing gradients and enable deeper feature hierarchies.
- **UNet-MTL** [31]: an encoder–decoder network with lateral skip connections that preserve fine-grained spatial details through multi-scale feature fusion.
- **SENet-MTL** [14]: a squeeze-and-excitation network that recalibrates channel-wise feature responses via learned attention weights, building upon the architecture used in the original SHAFTS framework [20].

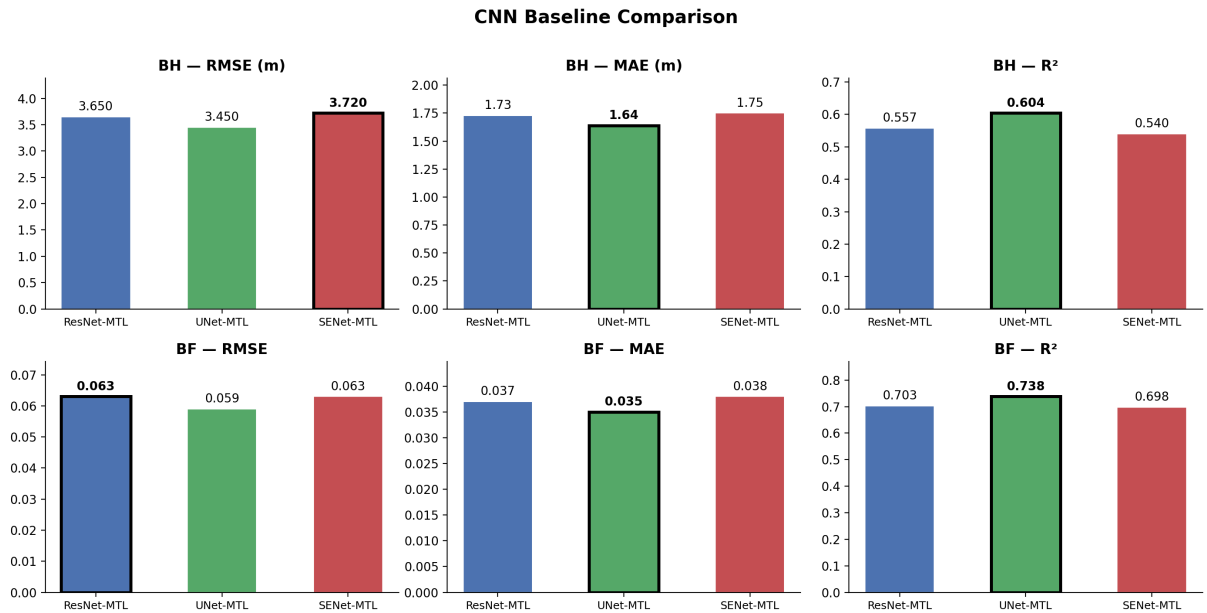


Figure 11: Comparison of three CNN baseline architectures on BH and BF prediction. UNet-MTL achieves the best overall performance across all metrics.

As shown in Figure 11, UNet-MTL consistently achieves the best performance among the three CNN baselines for both BH and BF tasks. Specifically, UNet-MTL yields BH RMSE of 3.45 m and  $R^2$  of 0.604, outperforming ResNet-MTL by 5.5% and SENet-MTL by 7.3% in RMSE. For BF prediction, UNet-MTL achieves the highest  $R^2$  (0.738) with the lowest RMSE (0.059). The performance ranking—UNet > ResNet > SENet—is consistent across both tasks, suggesting that the encoder–decoder feature pyramid in UNet provides a stronger inductive bias for dense spatial regression than either residual depth (ResNet) or channel attention alone (SENet).

Based on these results, UNet-MTL is selected as the strongest CNN baseline and is carried forward into all subsequent comparisons with GeoFormer.

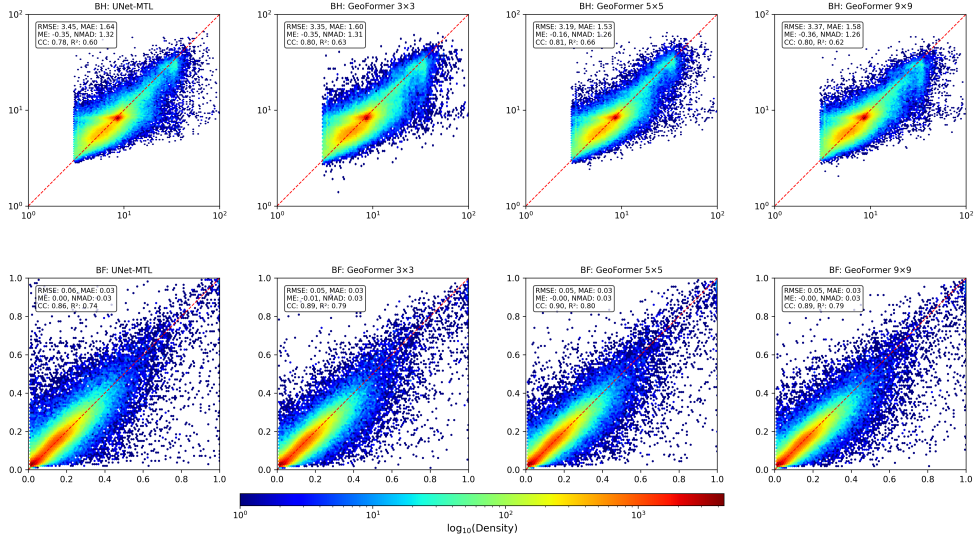


Figure 12: Scatter plots comparing predictions and ground truths for BH and BF under different receptive field configurations.

### 4.3 Experimental Results

To validate the effectiveness of the proposed **GeoFormer** framework, we compare it with the baseline model **UNet-MTL**, which was selected as the strongest CNN baseline in the preceding comparison. A detailed description of this model can be found in the Appendix.

As shown in Figure 12, the predicted values from GeoFormer are more tightly clustered along the identity line compared to the baseline UNet-MTL, indicating higher accuracy and reduced systematic bias. This effect is especially noticeable for the  $5 \times 5$  receptive field, which shows the densest distribution around the diagonal in both building height (BH, top row) and building footprint (BF, bottom row) panels.

In the BH panels, the baseline UNet-MTL tends to systematically underestimate taller buildings, particularly in the high-value range ( $> 30$  m), as evidenced by the visible skew below the red dashed line. GeoFormer significantly mitigates this bias, especially in the  $3 \times 3$  and  $5 \times 5$  configurations. The  $5 \times 5$  variant yields the lowest residual dispersion and the most symmetric pattern, suggesting superior generalization and robustness.

In the BF panels (bottom row), all GeoFormer variants produce denser clusters closer to the identity line, with the  $5 \times 5$  configuration again showing the strongest alignment. The color scale, indicating the logarithm of point density, confirms this improvement through brighter concentrations along the diagonal. This suggests not only improved accuracy but also fewer large outliers in footprint prediction.

Quantitative metrics that support these observations are presented in Table 5.

Table 5 summarizes the quantitative evaluation results for both building height (BH) and building footprint (BF) prediction across different receptive field configurations. The proposed GeoFormer consistently outperforms the baseline UNet-MTL across all metrics.

For BH prediction, GeoFormer with a  $5 \times 5$  receptive field achieves the lowest RMSE (3.19 m) and MAE (1.53 m), representing a relative reduction of 7.5% and 6.7%, respectively, compared to the baseline UNet-MTL (RMSE: 3.45 m, MAE: 1.64 m). Furthermore,

Table 5: Quantitative evaluation of BH and BF predictions across models and receptive fields.

Model	RMSE	MAE	ME	NMAD	CC	$R^2$
<i>Building Height (BH)</i>						
UNet-MTL	3.45	1.64	-0.35	1.32	0.78	0.60
GeoFormer 3×3	3.35	1.60	-0.35	1.31	0.80	0.63
GeoFormer 5×5	<b>3.19</b>	<b>1.53</b>	<b>-0.16</b>	<b>1.26</b>	<b>0.81</b>	<b>0.66</b>
GeoFormer 9×9	3.37	1.58	-0.36	1.26	0.80	0.62
<i>Building Footprint (BF)</i>						
UNet-MTL	0.06	0.03	0.00	0.03	0.86	0.74
GeoFormer 3×3	0.05	0.03	-0.01	0.03	0.89	0.79
GeoFormer 5×5	<b>0.05</b>	<b>0.03</b>	<b>0.00</b>	<b>0.03</b>	<b>0.90</b>	<b>0.80</b>
GeoFormer 9×9	0.05	0.03	0.00	0.03	0.89	0.79

the mean error (ME) is significantly closer to zero ( $-0.16$  vs.  $-0.35$ ), indicating reduced systematic bias. The NMAD also decreases from 1.32 to 1.26, demonstrating improved robustness to outliers. Importantly, the coefficient of determination ( $R^2$ ) rises from 0.60 to 0.66, and the Pearson correlation coefficient (CC) increases from 0.78 to 0.81, reflecting enhanced predictive consistency and structural fidelity.

In the BF regression task, improvements are also notable. The RMSE drops from 0.06 to 0.05, while the  $R^2$  improves from 0.74 to 0.80 and the CC from 0.86 to 0.90 for the  $5 \times 5$  configuration. This indicates that GeoFormer is not only more accurate in predicting average values but also better aligned with the spatial distribution patterns of both height and footprint metrics.

Overall, the  $5 \times 5$  receptive field configuration offers the most balanced trade-off between accuracy, robustness, and generalization, making it the optimal choice for both BH and BF tasks. In contrast, simply enlarging the receptive field to  $9 \times 9$  does not yield further gains and even slightly degrades performance in BH prediction (e.g., RMSE increases from 3.19 to 3.37). This may be attributed to over-smoothing effects caused by excessive contextual aggregation, which can dilute fine-grained spatial details critical for accurate estimation.

#### 4.4 Error Source Analysis

To complement the quantitative evaluation, we perform an in-depth analysis of prediction errors across different building characteristics. Residuals are stratified by height ( $H_{\text{ave}}$ ) and footprint density ( $\lambda_p$ ) to reveal patterns linked to sample rarity, spatial imbalance, and model-specific behavior.

Figure 13 presents the stratified error analysis for building height (BH) predictions, plotted over binned grids of average building height ( $H_{\text{ave}}$ ) and footprint density ( $\lambda_p$ ). The three panels respectively show the root mean square error (RMSE), mean error (ME), and normalized median absolute deviation (NMAD). A consistent trend is observed across all models: in regions where  $H_{\text{ave}} > 50$  m, both RMSE and NMAD increase substantially, highlighting the inherent difficulty of predicting rare high-rise buildings.

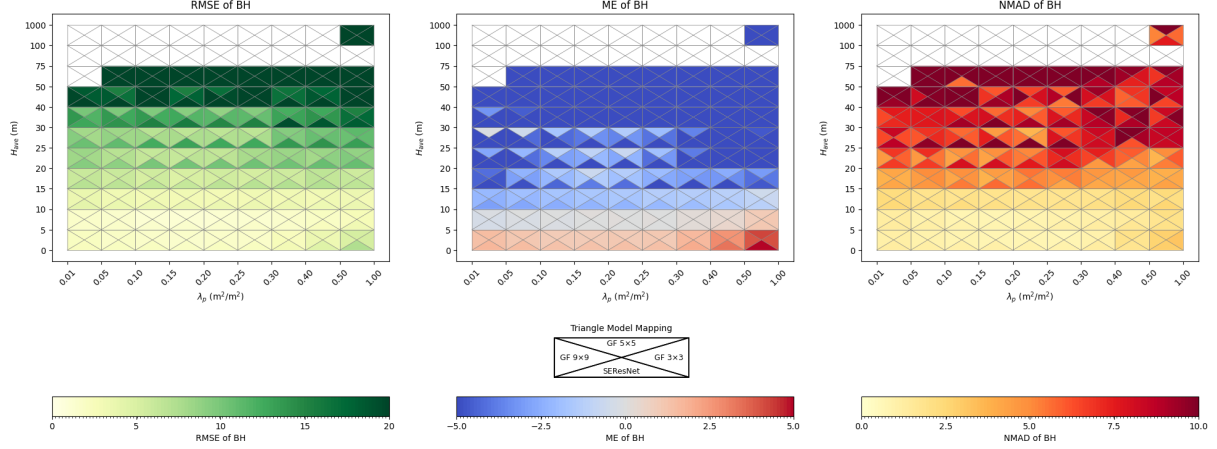


Figure 13: Stratified error analysis of building height prediction across height and density bins

Furthermore, the ME panel reveals that UNet-MTL and GeoFormer  $9 \times 9$  tend to exhibit stronger negative bias—i.e., underestimation—especially in these tall-building regions. This underperformance is likely due to limited representation of such samples in the training data. In contrast, the GeoFormer variants with  $5 \times 5$  and  $3 \times 3$  receptive fields demonstrate better calibration, with lower errors and reduced bias. These results collectively indicate that smaller receptive fields help preserve critical spatial details and improve robustness when dealing with vertical complexity.

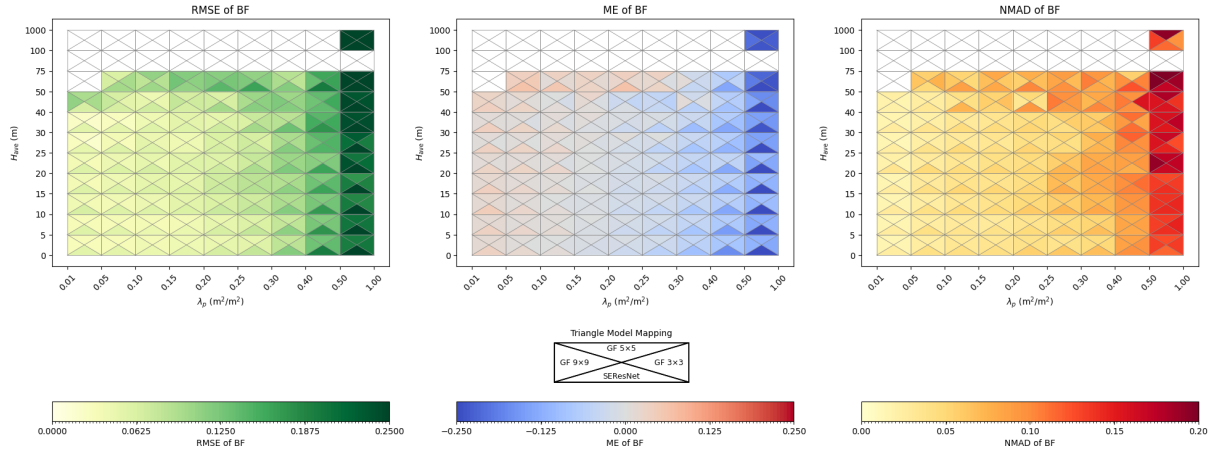


Figure 14: Stratified error analysis of building footprint prediction across height and density bins

Figure 14 illustrates the stratified error maps for building footprint (BF) predictions across the same binned space of average building height ( $H_{ave}$ ) and footprint density ( $\lambda_p$ ). A notable pattern emerges: prediction errors, particularly RMSE and NMAD, increase markedly in regions with high planar density ( $\lambda_p > 0.5$ ), indicating that all models face difficulty in densely built environments.

The ME plot further reveals a consistent underestimation trend across models in these high-density regions. This systematic negative bias may be attributed to the scarcity of compact patches in the training dataset, which leads to poorer generalization in these cases. Among the evaluated models, GeoFormer with a  $5 \times 5$  receptive field exhibits the

most stable and balanced performance, maintaining lower errors and reduced bias even under extreme density conditions. This suggests that moderate contextual aggregation improves footprint estimation while avoiding the over-smoothing observed in larger receptive fields.

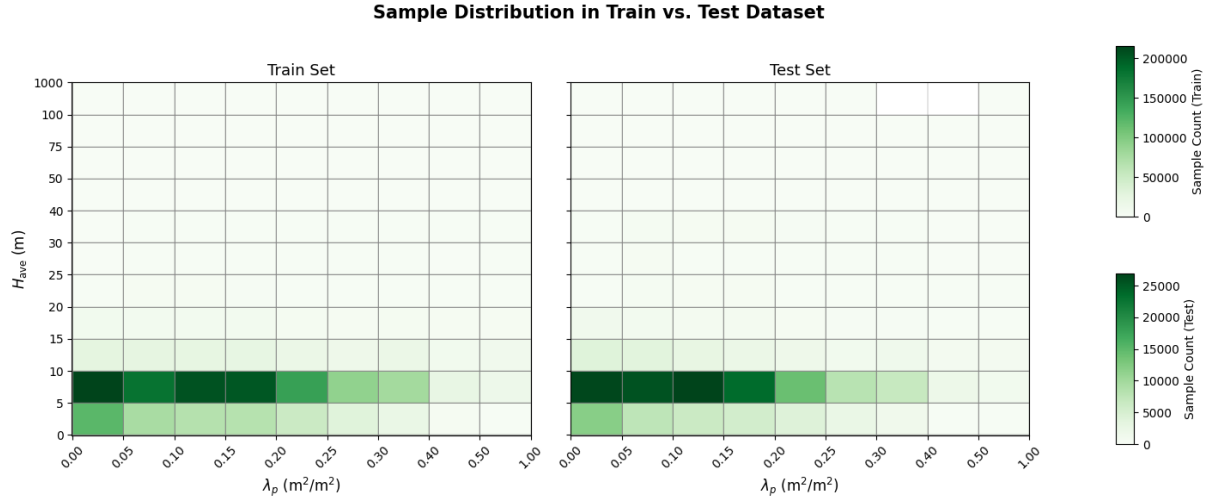


Figure 15: Sample distribution in train vs. test dataset.

Figure 15 illustrates the joint distribution of building height ( $H_{\text{ave}}$ ) and footprint ratio ( $\lambda_p$ ) in the train and test datasets. A pronounced long-tailed pattern is observed, where samples with  $H_{\text{ave}} > 30$  m and  $\lambda_p > 0.7$  are extremely rare, accounting for only 1.1% and 0.54% of the total data, respectively. This imbalance explains the model’s degraded performance in high-rise and dense areas, as the network receives insufficient training signals from these underrepresented regimes. In fact, the model performs robustly on the majority of cases, and the main bottleneck lies not in architectural flaws, but in data coverage. Future efforts should prioritize collecting more representative samples from vertical and compact urban environments to improve generalization.

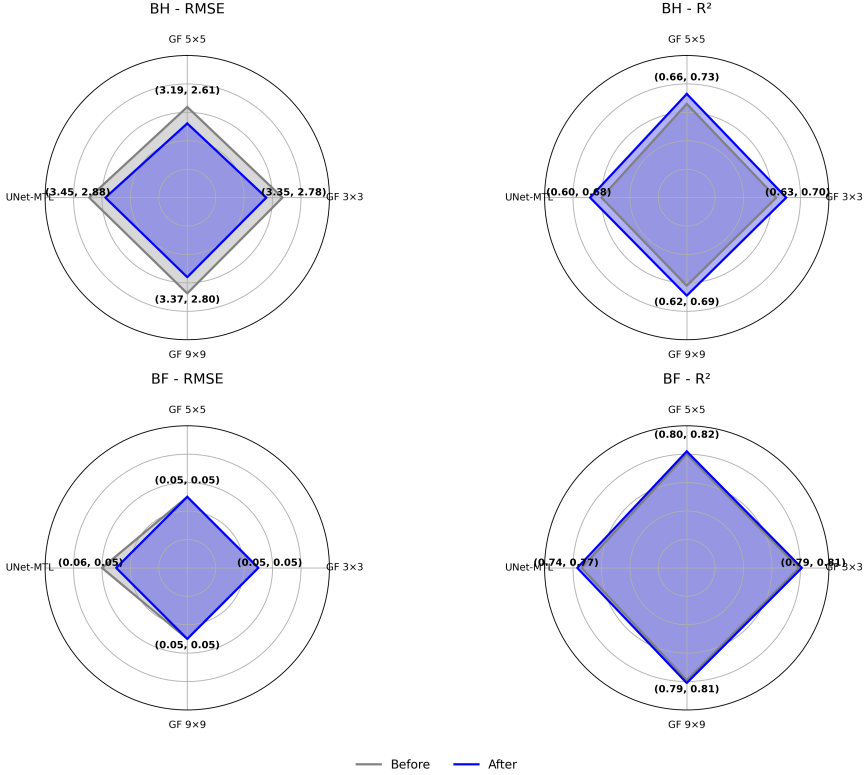


Figure 16: Performance before and after removing the top 0.1% residuals across four model configurations for BH and BF estimation.

To mitigate the impact of extreme prediction errors, we further removed the top 0.1% of residuals from each model’s output. As shown in Fig. 16, this adjustment led to consistent improvements in both RMSE and  $R^2$  metrics across all model configurations. The enhancement was particularly notable for building height (BH) prediction, indicating that tall buildings often constitute the most outlying errors in the residual distribution.

Overall, the GeoFormer series exhibited more stable and consistent improvements after outlier removal, especially in configurations with larger receptive fields ( $5 \times 5$  and  $9 \times 9$ ). This suggests that incorporating broader spatial context plays a critical role in suppressing localized prediction anomalies.

In summary, removing extreme residuals helps reveal the core predictive capacity of each model and highlights the importance of model structure in ensuring robustness.

## 5 Ablation Study

To systematically evaluate the design choices underlying GeoFormer, we conduct four ablation experiments organised into two groups: **structural ablation** (model capacity and DEM removal) and **modality ablation** (SAR and optical channel removal). All ablation variants share the same training protocol and GeoSplit partitioning as the full GeoFormer ( $5 \times 5$ ) model, differing only in the factor under investigation.

## 5.1 Structural Ablation

### 5.1.1 Effect of Model Capacity (Enlarged Model)

A natural hypothesis is that increasing model capacity should improve prediction accuracy. To test this, we train an *Enlarged* GeoFormer variant in which the Swin Transformer embedding dimension and depth are doubled relative to the baseline configuration, roughly quadrupling the number of trainable parameters. Table 6 shows the results on the three-city held-out test set.

The Enlarged model achieves noticeably lower training error (BH RMSE 2.53 m vs. 3.28 m for the baseline), yet its test-set BH RMSE increases to 3.34 m compared with 3.19 m for the standard model, and the BH  $R^2$  drops from 0.661 to 0.629. As illustrated in Fig. 17, the widening train–test gap in the Enlarged model constitutes clear evidence of overfitting: the extra parameters memorise training-set specifics rather than learning generalisable urban morphology features. This finding justifies the compact architecture adopted for the final GeoFormer model.

### 5.1.2 Effect of Removing the DEM Channel

DEM encodes local terrain elevation, which is conceptually correlated with building height. To quantify its contribution, we retrain GeoFormer with DEM removed from the input stack, retaining only SAR and optical channels. As shown in Table 6, removing DEM leads to the largest BH degradation among all ablation variants: BH RMSE rises from 3.19 m to 3.67 m (+15.0 %) and BH  $R^2$  falls from 0.661 to 0.552 (−16.5 %). In contrast, BF RMSE increases only marginally (0.051 to 0.052).

This asymmetric impact confirms that DEM provides essential vertical-scale cues for height estimation but contributes little to planar footprint prediction, where spectral and textural information already suffice.

Table 6: Structural ablation results on the three-city held-out test set.

Model	Building Height			Building Footprint		
	MAE	RMSE	$R^2$	MAE	RMSE	$R^2$
GeoFormer (Full)	1.44	3.19	0.661	0.031	0.051	0.801
Enlarged	1.52	3.34	0.629	0.029	0.048	0.823
Without DEM	1.68	3.67	0.552	0.032	0.052	0.794

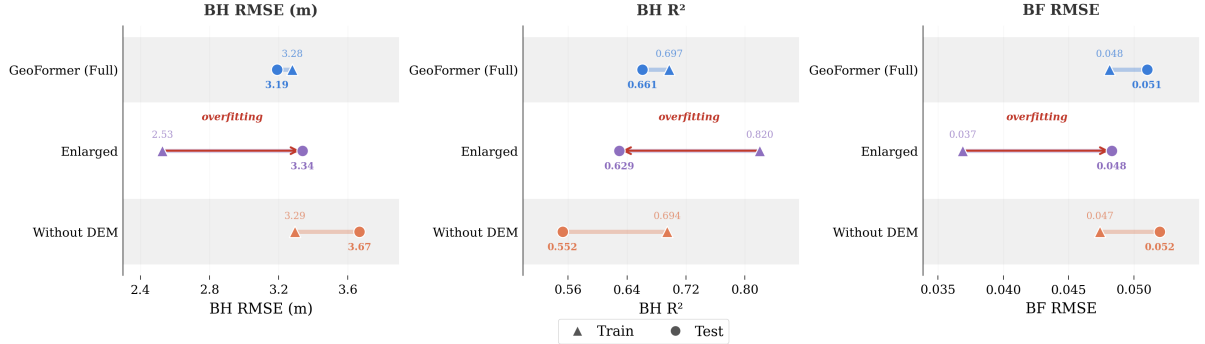


Figure 17: Train vs. test performance gap for GeoFormer (Full), Enlarged, and Without-DEM variants. The Enlarged model exhibits a clear overfitting pattern: substantially lower training error but higher test error.

## 5.2 Modality Ablation

### 5.2.1 Effect of Removing the SAR Channel (No-SAR)

To assess the contribution of SAR backscatter, we train GeoFormer with only Sentinel-2 optical and DEM inputs. As reported in Table 7, removing SAR incurs a moderate degradation in BH performance (RMSE: 3.19 → 3.38 m, +6.0 %), while BF RMSE shows a somewhat larger relative increase (0.051 → 0.059, +15.7 %). This suggests that SAR’s primary contribution lies in capturing three-dimensional scattering features related to structural density, which are not fully captured by optical reflectance alone.

### 5.2.2 Effect of Removing the Optical Channel (No-Optical)

Conversely, removing Sentinel-2 optical data and retaining only SAR and DEM results in a dramatically larger performance drop. BH RMSE increases to 4.40 m (+37.9 %), BH R<sup>2</sup> collapses from 0.661 to 0.357, and BF RMSE rises to 0.074 (+45.1 %). The No-Optical model consistently exhibits the highest validation MAE throughout training (Fig. 18), confirming that multispectral reflectance is the dominant information source for both height and footprint retrieval at 100 m resolution.

Table 7: Modality ablation results evaluated on the 51-city global test set (Test2).

Configuration	Building Height			Building Footprint		
	MAE	RMSE	R <sup>2</sup>	MAE	RMSE	R <sup>2</sup>
GeoFormer (Full)	1.53	3.19	0.661	0.031	0.051	0.801
No-SAR (Opt+DEM)	1.62	3.38	0.620	0.036	0.059	0.735
No-Optical (SAR+DEM)	2.14	4.40	0.357	0.047	0.074	0.581

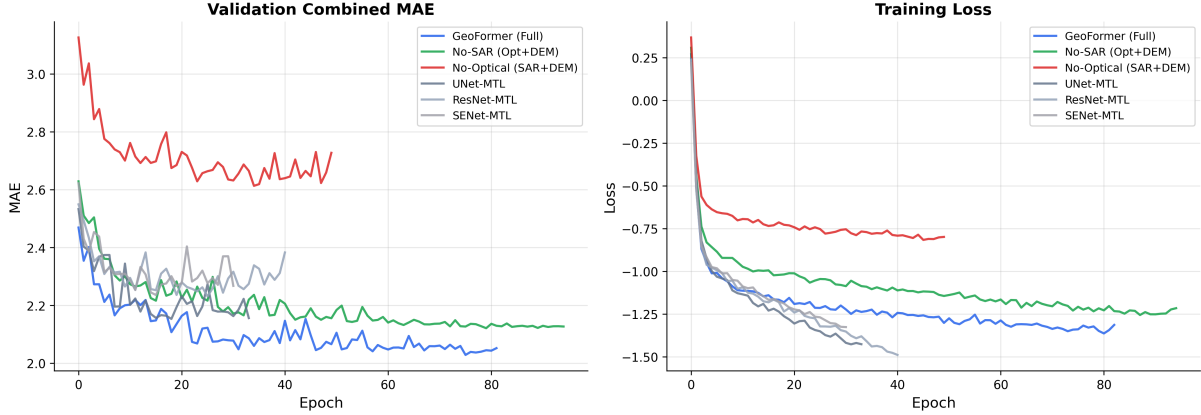


Figure 18: Validation combined MAE and training loss curves for GeoFormer variants and CNN baselines. All runs were configured for 150 epochs but terminated earlier by the early-stopping mechanism (patience = 10 on validation  $R^2$ ), hence the varying curve lengths. The No-Optical configuration consistently exhibits higher error, while the full model and No-SAR variant converge to similar levels.

### 5.3 Summary of Ablation Findings

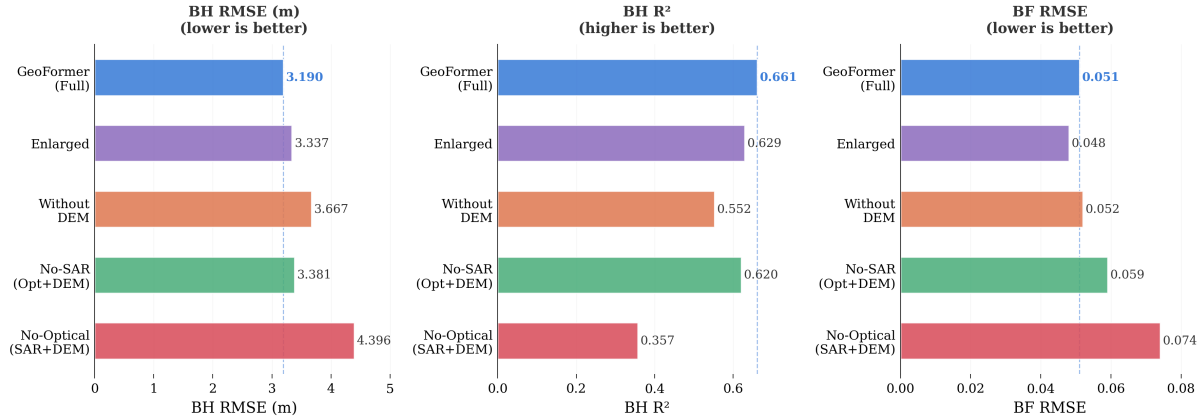


Figure 19: Consolidated comparison of all ablation variants. Top row: structural ablation (capacity and DEM); bottom row: modality ablation (SAR and optical).

Figure 19 consolidates the results from all four ablation experiments. Three principal conclusions emerge:

1. **Model capacity must be carefully calibrated.** The Enlarged variant achieves lower training error but higher test error, demonstrating that naively scaling model parameters leads to overfitting rather than improved generalisation in this data regime.
2. **DEM is indispensable for height estimation.** Removing DEM causes the largest single-factor degradation in BH metrics (+15.0 % RMSE, -16.5 %  $R^2$ ) while barely affecting BF, confirming that topographic context provides unique vertical-scale information not recoverable from spectral data alone.

3. **Optical imagery is the dominant modality.** The No-Optical configuration suffers the most severe performance collapse across all metrics (+37.9 % BH RMSE). By contrast, removing SAR causes only moderate degradation (+6.0 % BH RMSE), indicating that multispectral reflectance carries the primary predictive signal at 100 m resolution. Nevertheless, the full SAR+Optical+DEM model remains the top performer, validating the complementary value of multi-source fusion.

## 6 Evaluating Model Generalization

### 6.1 Cross-Dataset Generalization: Test on Suwon, Korea

To evaluate GeoFormer’s generalization beyond the training domain, we test its performance on Suwon, South Korea—a large East Asian city with distinct morphology and sensor conditions. Unlike the high-rise, hyper-dense cores in the training data, Suwon features a diverse mix of mid-rise residences, low-rise industry, and historical structures, providing a challenging out-of-distribution benchmark. All input features follow the same pre-processing pipeline as Sec. 2, while reference labels were sourced from Korea’s national 3D mapping program. Notably, building height attributes are incomplete: only 30% of footprints have valid height entries, highlighting the practical challenge of sparse supervision in new cities.

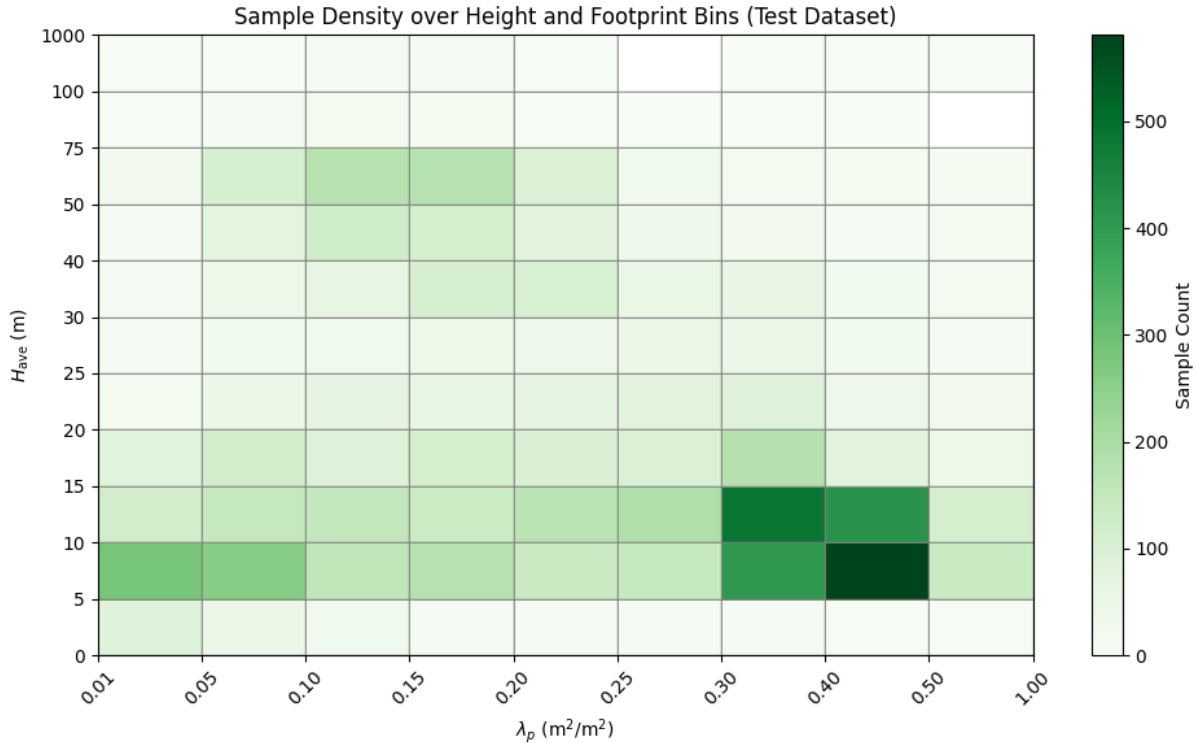


Figure 20: Joint distribution of building height and footprint in Suwon.

According to a nationwide statistical analysis of 229 administrative regions in South Korea, the average building height is 10.07 m [19]. To construct a representative evaluation subset, we analysed the joint distribution of building height (BH) and building footprint (BF) within Suwon. As shown in Figure 20, the majority of samples are concentrated

within the BH range of 5–15 m and the BF range of 0.01–0.5. The BH range was chosen to avoid the influence of large deviations caused by extremely tall buildings with missing or inaccurate labels, while the BF range captures the densest portion of the distribution, ensuring statistical robustness. This subset reflects mid-rise, moderately dense urban structures and serves as a practical testbed for evaluating the model’s generalisation capability.

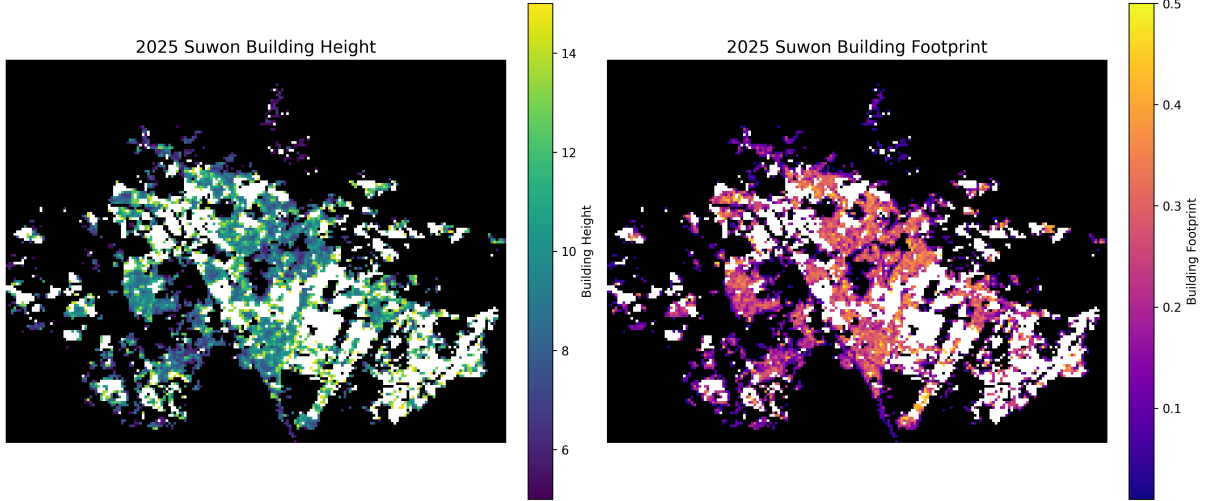


Figure 21: Spatial distribution of building height (left) and footprint (right) in Suwon for the evaluation subset ( $5 \leq H_{\text{ave}} < 15$  m and  $0.01 \leq \lambda_p < 0.5$ ). Colored pixels indicate selected grid cells.

Figure 21 illustrates the spatial distribution of building height (left) and footprint (right) in Suwon for the selected evaluation subset. The colored pixels denote grid cells that meet the selection criteria of  $5 \leq H_{\text{ave}} < 15$  m and  $0.01 \leq \lambda_p < 0.5$ . This subset covers both central and peripheral regions of the city, ensuring a diverse morphological composition.

Table 8: Model performance on the Suwon subset defined by  $0.01 \leq \lambda_p < 0.5$  and  $5 \leq H_{\text{ave}} < 15$  m.

Metric	Building Height	Building Footprint
RMSE	3.573 m	0.126
MAE	2.655 m	0.100
# Samples	3 710	(62.55 % of total)

We evaluated the best-performing GeoFormer model variant ( $5 \times 5$  contextual window) on this subset. As shown in Table 8, the model achieved an RMSE of 3.573 m for building height and 0.126 for building footprint, across 3,710 samples (62.55% of the test set). These results validate the model’s capacity to generalize across urban typologies in Suwon.

This geographically balanced sampling strategy enables a more rigorous evaluation of cross-domain generalization. By including both dense residential blocks and low-rise peripheral areas, it ensures that model performance is not inflated by spatially homogeneous regions. More importantly, the strong results on this subset demonstrate that the model

maintains high accuracy even when applied to an *unseen city* exhibiting distinct morphological and sensor characteristics compared to the training domains. This highlights the model’s ability to generalize beyond distributional boundaries, validating its robustness under real-world domain shifts and spatial heterogeneity.

## 6.2 Exploring Model Potential in Earthquake-Affected Regions of Turkey

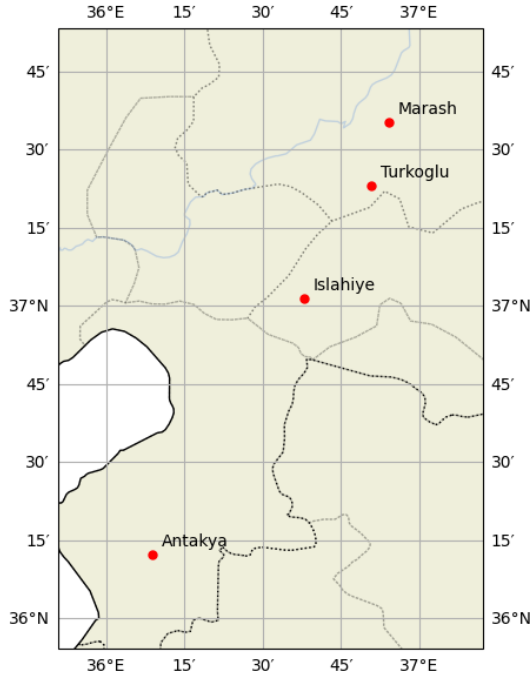


Figure 22: Geographic locations of the four selected cities in southern Turkey

To illustrate the model’s real-world utility, GeoFormer was deployed over four cities—Marash, Turkoglu, Islahiye, and Antakya—heavily damaged by the 2023 Kahramanmaraş earthquakes in southern Turkey (Fig. 22). For each city, paired Sentinel-1/2 scenes acquired within one month before and after the event were processed on a 100 m grid; no fine-tuning was applied.

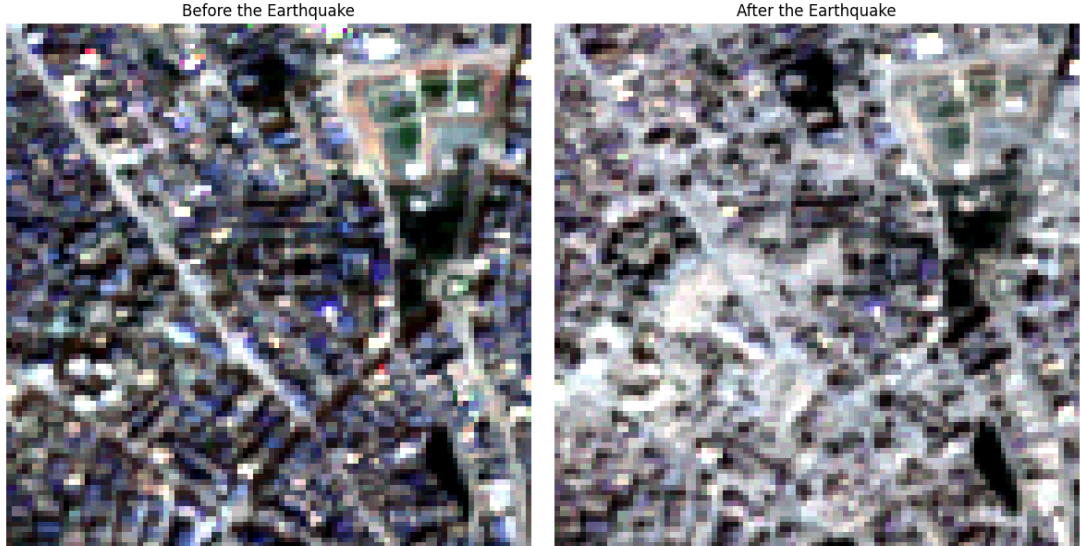


Figure 23: Sentinel-2 images of Antakya before and after the 2023 earthquake

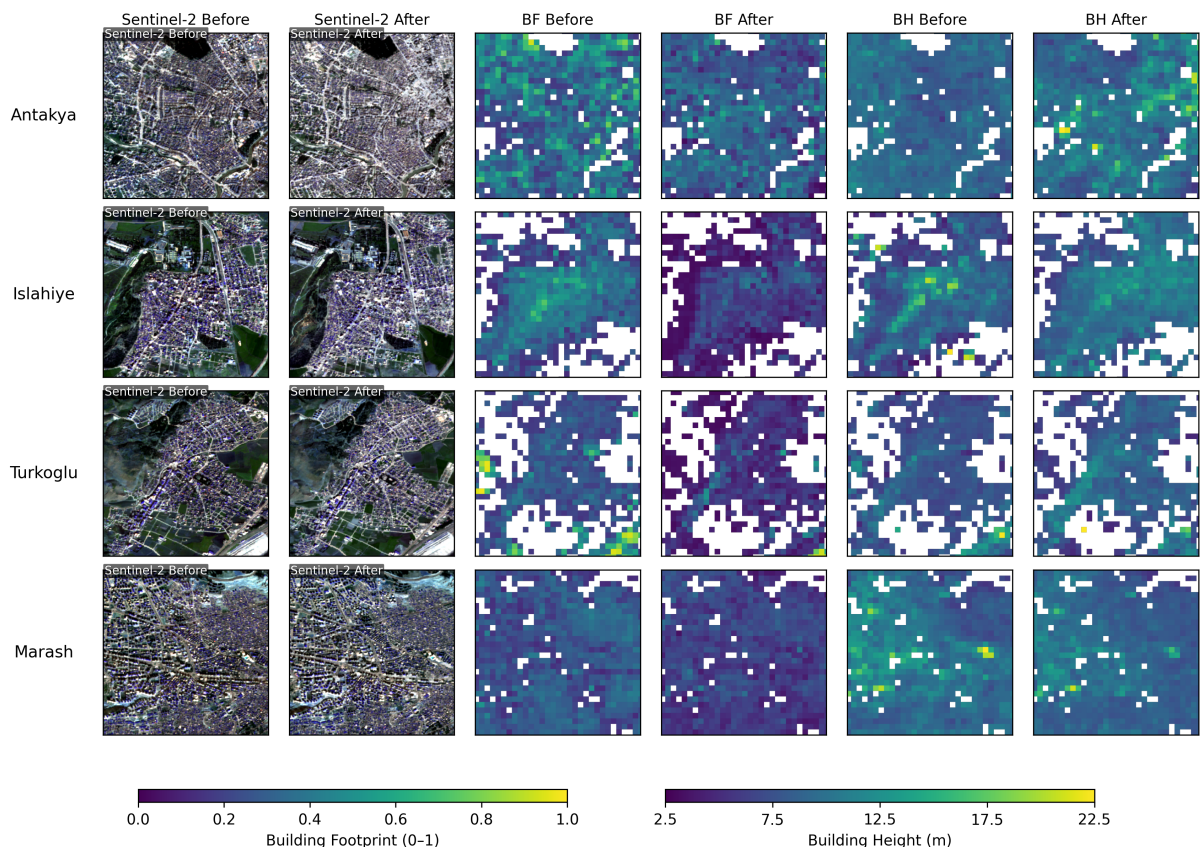


Figure 24: Pre- and post-earthquake Sentinel-2 imagery and predicted BF/BH for four affected cities

Figure 23 contrasts pre- and post-quake Sentinel-2 imagery in Antakya, where the loss of regular textures and the emergence of bright, chaotic patterns visibly mark large-scale collapse.

To perform quantitative evaluation under noisy or uncertain labels, we restrict analysis

to urbanized areas where building morphological patterns are more stable and reliable. To achieve this, we implement a post-processing procedure based on the City Clustering Algorithm using percolation theory (CCAP) [4]. This method automatically determines an optimal threshold  $\lambda_p^*$  on the building footprint (BF) map, enabling the separation of urban versus non-urban regions in a data-driven manner.

Specifically, a set of candidate BF thresholds  $\{\lambda_{p_i}\}$  with uniform spacing is evaluated. For each threshold, a binary mask is generated by marking pixels that satisfy both  $\text{BF} \geq \lambda_{p_i}$  and  $\text{BH} \geq 5.0 \text{ m}$ . Urban clusters are then identified via 4-connectivity labeling, and the entropy of cluster size distribution is computed. The optimal threshold  $\lambda_p^*$  is chosen to maximize this entropy, thereby favoring spatially coherent and diverse urban forms:

$$\lambda_p^* = \arg \max_i \text{Entropy}(\lambda_{p_i}).$$

In our implementation, thresholds are sampled from  $\lambda_p \in [0.005, 0.15]$  with 30 uniform steps, and the entropy penalty term is regularized to avoid over-expansion. The resulting CCAP mask is used throughout the evaluation to suppress peripheral and noisy areas, ensuring more robust and meaningful comparisons before and after the event.

Table 9: Mean values of predicted building footprint (BF) and building height (BH) before and after the 2023 earthquake across four affected cities (within  $\pm 1.5 \text{ km}$  of city center).

City	BF Before	BF After	BH Before	BH After
Antakya	0.3721	0.2976	9.22	10.20
Islahiye	0.3148	0.1417	8.60	9.66
Turkoglu	0.2960	0.1435	7.97	8.49
Marash	0.2681	0.1912	10.04	9.17
<b>Overall</b>	0.3128	0.1935	8.96	9.38

A full comparison of model outputs is presented in Fig. 24. While building footprint (BF) exhibits consistent reductions across all four city cores, indicating significant loss of built-up structures, changes in building height (BH) are more heterogeneous. In particular, some cities show an increase in mean BH following the earthquake.

Table 9 summarizes the mean BF and BH values within a  $\pm 1.5 \text{ km}$  radius of each city center. BF decreased in all cities—for example, Islahiye experienced a 55% reduction—whereas BH increased in three of the four cases. This counterintuitive trend is explained by two interacting factors: (i) collapsed buildings tend to lose their structural and spectral signatures in satellite imagery and are thus masked out during evaluation, and (ii) low-rise, seismically vulnerable structures are more likely to be destroyed, effectively removing lower height values from the calculation. As a result, the mean BH of the remaining, typically taller structures increases.

These findings underscore GeoFormer’s ability not only to detect explicit reductions in urban density but also to reflect more subtle shifts in the vertical morphology of the built environment. Such sensitivity to both direct damage and structural redistribution enhances the model’s value in post-disaster diagnostics.

## 7 Conclusion

This study introduces **GeoFormer**, a scalable Transformer-based framework for joint estimation of building height (BH) and building footprint (BF) at 100 m resolution. Leveraging only globally available Sentinel-1, Sentinel-2, and DEM data, GeoFormer addresses key challenges in 3D urban mapping by eliminating reliance on proprietary VHR inputs, integrating vertical information, and enhancing scene-level generalisation.

A core contribution lies in the adoption of a *geo-blocked* data-splitting strategy that ensures strict spatial separation between training and evaluation areas. Built upon a Swin Transformer backbone and structured as a multi-task learning model, GeoFormer systematically investigates context window sizes ( $3 \times 3$ ,  $5 \times 5$ ,  $9 \times 9$ ), identifying  $5 \times 5$  (500 m) as optimal in balancing accuracy and efficiency.

Evaluation on 54 morphologically diverse cities demonstrates that GeoFormer achieves robust generalisation performance. In held-out test regions spanning multiple continents, the model attains a building height RMSE of 3.19 m and a building footprint RMSE of 0.051, reducing BF prediction error by over 37 % compared to the best CNN baseline (UNet-MTL). Cross-dataset transfer to Suwon, Korea—a city not seen during training—yields a BH RMSE below 3.5 m, confirming the model’s ability to generalise across distinct urban morphologies and geographic contexts.

Comprehensive ablation studies provide several critical architectural insights:

1. **Model capacity must be carefully calibrated.** Increasing model parameters beyond a compact configuration leads to pronounced overfitting, with training-to-test performance gaps widening across all metrics.
2. **DEM is indispensable for height estimation.** Removing DEM causes the largest single-factor degradation in BH metrics (+15.0 % RMSE,  $-16.5\%$   $R^2$ ) while barely affecting BF, confirming that topographic context provides unique vertical-scale information not recoverable from spectral data alone.
3. **Optical imagery is the dominant modality.** The No-Optical configuration suffers the most severe performance collapse (+37.9 % BH RMSE,  $-46.0\%$   $R^2$ ), whereas removing SAR causes only moderate degradation (+6.0 % BH RMSE). This indicates that multispectral reflectance carries the primary predictive signal at 100 m resolution. Nevertheless, the full SAR+Optical+DEM model remains the top performer, validating the complementary value of multi-source fusion.

Furthermore, a case study on the 2023 Türkiye–Syria earthquake demonstrates GeoFormer’s potential for post-disaster damage assessment. The model successfully detects reductions in building footprint across all affected cities and reveals counterintuitive increases in mean building height—attributable to the selective collapse of low-rise structures—thereby showcasing its sensitivity to both overt structural loss and subtle morphological redistribution.

Looking forward, future work may explore fine-grained decoding mechanisms such as super-resolution modules or graph-based refinement to translate 100 m predictions to per-building scale. Incorporating multi-temporal satellite sequences could support dynamic monitoring of urban growth and disaster impact. Additionally, the modality-specific insights from our ablation study suggest that adaptive fusion strategies—where sensor con-

tributions are weighted according to geographic context—may further improve global-scale performance. Together, these directions extend the utility of GeoFormer to applications in urban resilience, climate adaptation, and geospatial intelligence.

## Acknowledgement

This research was supported by the 2023-MOIS36-004 (RS-2023-00248092) of the Technology Development Program on Disaster Restoration Capacity Building and Strengthening funded by the Ministry of Interior and Safety (MOIS, Korea).

## Data Availability Statement

The training dataset , trained model weights, and source code for the GeoFormer framework are publicly available. The dataset is archived on Zenodo at <https://doi.org/10.5281/zenodo.185738> and the source code is hosted on GitHub at <https://github.com/geumjin99/geoformer>.

## Declaration of Competing Interests

The authors declare that they have no known competing financial interests or personal relationships that could have appeared to influence the work reported in this paper.

## References

- [1] Benjamin Bechtel, Klemen Zakšek, and Gholamali Hoshyaripour. Downscaling land surface temperature in an urban area: A case study for Hamburg, Germany. *Remote Sens.*, 4(10):3184–3200, 2012.
- [2] Mehmet Buyukdemircioglu, Recep Can, Sultan Kocaman, and Martin Kada. Deep learning based building footprint extraction from very high resolution true orthophotos and nDSM. *ISPRS Ann. Photogramm. Remote Sens. Spat. Inf. Sci.*, 2:211–218, 2022.
- [3] Bowen Cai, Zhenfeng Shao, Xiao Huang, Xuechao Zhou, and Shenghui Fang. Deep learning-based building height mapping using Sentinel-1 and Sentinel-2 data. *Int. J. Appl. Earth Obs. Geoinformation*, 122:103399, 2023.
- [4] Wenpu Cao, Lei Dong, Lun Wu, and Yu Liu. Quantifying urban areas with multi-source data based on percolation theory. *Remote Sens. Environ.*, 241:111730, 2020.
- [5] Yuehong Chen, Jiayue Zhou, Congcong Xu, Qiang Ma, Xiaoxiang Zhang, Ya’nan Zhou, and Yong Ge. Structure-aware deep learning network for building height estimation. *Int. J. Appl. Earth Obs. Geoinformation*, page 104443, 2025.
- [6] Kristina Dabrock, Noah Pflugradt, Jann Michael Weinand, and Detlef Stolten. Leveraging machine learning to generate a unified and complete building height dataset for Germany. *Energy AI*, 17:100408, 2024.

[7] Matthias Demuzere, Jonas Kittner, Alberto Martilli, Gerald Mills, Christian Moede, Iain D Stewart, Jasper Van Vliet, and Benjamin Bechtel. A global map of Local Climate Zones to support earth system modelling and urban scale environmental science. *Earth Syst. Sci. Data Discuss.*, 2022:1–57, 2022.

[8] Chuanglin Fang, Guangdong Li, and Shaojian Wang. Changing and differentiated urban landscape in China: Spatiotemporal patterns and driving forces. *Environ. Sci. Technol.*, 50(5):2217–2227, 2016.

[9] David Frantz, Franz Schug, Akpona Okujeni, Claudio Navacchi, Wolfgang Wagner, Sebastian van der Linden, and Patrick Hostert. National-scale mapping of building height using Sentinel-1 and Sentinel-2 time series. *Remote Sens. Environ.*, 252: 112128, 2021.

[10] Steve Frolking, Tom Milliman, Karen C Seto, and Mark A Friedl. A global fingerprint of macro-scale changes in urban structure from 1999 to 2009. *Environ. Res. Lett.*, 8 (2):024004, 2013.

[11] Steve Frolking, Richa Mahtta, Tom Milliman, Thomas Esch, and Karen C Seto. Global urban structural growth shows a profound shift from spreading out to building up. *Nat. Cities*, 1(9):555–566, 2024.

[12] Geofabrik. OpenStreetMap download statistics, 2018.

[13] Kaiming He, Xiangyu Zhang, Shaoqing Ren, and Jian Sun. Deep residual learning for image recognition. In *Proc. IEEE Conf. Comput. Vis. Pattern Recognit.*, pages 770–778, 2016.

[14] Jie Hu, Li Shen, and Gang Sun. Squeeze-and-excitation networks. In *Proc. IEEE Conf. Comput. Vis. Pattern Recognit.*, pages 7132–7141, 2018.

[15] Xiao Huang and Cuizhen Wang. Estimates of exposure to the 100-year floods in the conterminous United States using national building footprints. *Int. J. Disaster Risk Reduct.*, 50:101731, 2020.

[16] Peter J Huber. Robust estimation of a location parameter: Annals mathematics statistics, 35. *Ji Xue Carin L2008‘Bayesian Compressive Sensing’ IEEE Trans. Signal Process.*, 56(6):2346–2356, 1964.

[17] Alex Kendall, Yarin Gal, and Roberto Cipolla. Multi-task learning using uncertainty to weigh losses for scene geometry and semantics. In *Proc. IEEE Conf. Comput. Vis. Pattern Recognit.*, pages 7482–7491, 2018.

[18] Yu Ting Kwok, Cecile De Munck, Robert Schoetter, Chao Ren, and Kevin Ka-Lun Lau. Refined dataset to describe the complex urban environment of Hong Kong for urban climate modelling studies at the mesoscale. *Theor. Appl. Climatol.*, 142(1): 129–150, 2020.

[19] Min-Hyung Lee, Woo-Seok Seo, Chang-Young Park, and Chang-Ho Choi. Improvement of surface roughness classification criteria reflecting the height and density of building by region. *J. Korean Inst. Archit. Sustain. Environ. Build. Syst. KIAEBS*, 15(5):513–524, 2021.

[20] Ruidong Li, Ting Sun, Fuqiang Tian, and Guang-Heng Ni. SHAFTS (v2022.3): A deep-learning-based Python package for simultaneous extraction of building height and footprint from Sentinel imagery. *Geosci. Model Dev.*, 16(2):751–778, 2023. doi: 10.5194/gmd-16-751-2023.

[21] Xuecao Li, Yuyu Zhou, Peng Gong, Karen C Seto, and Nicholas Clinton. Developing a method to estimate building height from Sentinel-1 data. *Remote Sens. Environ.*, 240:111705, 2020.

[22] Ziming Li, Qinchuan Xin, Ying Sun, and Mengying Cao. A deep learning-based framework for automated extraction of building footprint polygons from very high-resolution aerial imagery. *Remote Sens.*, 13(18):3630, 2021.

[23] Ze Liu, Yutong Lin, Yue Cao, Han Hu, Yixuan Wei, Zheng Zhang, Stephen Lin, and Baining Guo. Swin transformer: Hierarchical vision transformer using shifted windows. In *Proc. IEEE/CVF Int. Conf. Comput. Vis.*, pages 10012–10022, 2021.

[24] Ilya Loshchilov and Frank Hutter. Sgdr: Stochastic gradient descent with warm restarts. *ArXiv Prepr. ArXiv160803983*, 2016.

[25] Ilya Loshchilov and Frank Hutter. Decoupled weight decay regularization. *ArXiv Prepr. ArXiv171105101*, 2017.

[26] Fatemeh Mostafavi et al. GLObal Building heights for Urban Studies (UT-GLOBUS) for city- and street-scale urban simulations: Development and first applications. *Scientific Data*, 11:866, 2024. doi: 10.1038/s41597-024-03719-w.

[27] Łukasz Musiaka and Marta Nalej. Application of GIS tools in the measurement analysis of urban spatial layouts using the square grid method. *ISPRS Int. J. Geo-Inf.*, 10(8):558, 2021. doi: 10.3390/ijgi10080558.

[28] Katia Perini and Adriano Magliocco. Effects of vegetation, urban density, building height, and atmospheric conditions on local temperatures and thermal comfort. *Urban For. Urban Green.*, 13(3):495–506, 2014.

[29] Meng Qi, Chunxue Xu, Wenwen Zhang, Matthias Demuzere, Perry Hystad, Tianjun Lu, Peter James, Benjamin Bechtel, and Steve Hankey. Mapping urban form into local climate zones for the continental US from 1986–2020. *Sci. Data*, 11(1):195, 2024.

[30] Julien Radoux, Guillaume Chomé, Damien Christophe Jacques, François Waldner, Nicolas Bellemans, Nicolas Matton, Céline Lamarche, Raphaël d’Andrimont, and Pierre Defourny. Sentinel-2’s potential for sub-pixel landscape feature detection. *Remote Sens.*, 8(6):488, 2016.

[31] Olaf Ronneberger, Philipp Fischer, and Thomas Brox. U-net: Convolutional networks for biomedical image segmentation. In *Int. Conf. Med. Image Comput. Comput.-Assist. Interv.*, pages 234–241. Springer, 2015.

[32] Franz Schug, David Frantz, Akpona Okujeni, and Patrick Hostert. Sub-pixel building area mapping based on synthetic training data and regression-based unmixing using Sentinel-1 and-2 data. *Remote Sens. Lett.*, 13(8):822–832, 2022.

- [33] Yuan Tian, Minting Lu, Zhen Xu, and Jingyi Ren. A fire following earthquake spread model considering building height and its application to real-world events. *Int. J. Disaster Risk Reduct.*, page 105261, 2025.
- [34] Zhongchang Wang et al. MF-BHNet: A hybrid multimodal fusion network for building height estimation using Sentinel-1 and Sentinel-2 imagery. *IEEE Transactions on Geoscience and Remote Sensing*, 62:4512419, 2024. doi: 10.1109/TGRS.2024.3468502.
- [35] Wan-Ben Wu, Jun Ma, Ellen Banzhaf, Michael E Meadows, Zhao-Wu Yu, Feng-Xiang Guo, Dhritiraj Sengupta, Xing-Xing Cai, and Bin Zhao. A first Chinese building height estimate at 10 m resolution (CNBH-10 m) using multi-source earth observations and machine learning. *Remote Sens. Environ.*, 291:113578, 2023.
- [36] Chang Xi, Chen Ren, Junqi Wang, Zhuangbo Feng, and Shi-Jie Cao. Impacts of urban-scale building height diversity on urban climates: A case study of Nanjing, China. *Energy Build.*, 251:111350, 2021.
- [37] Yongjiu Zheng et al. Estimating individual building heights by integrating spaceborne LiDAR and multisource remote sensing data: A CNN–transformer model and a semi-supervised sample augmentation approach. *IEEE Transactions on Geoscience and Remote Sensing*, 63, 2025. doi: 10.1109/TGRS.2025.3601205.
- [38] Xiaoxiang Zhu, Sining Chen, Fahong Zhang, Yilei Shi, and Yuanyuan Wang. GlobalBuildingAtlas: An open global and complete dataset of building polygons, heights and LoD1 3D models. *Earth System Science Data*, 17:6647–6670, 2025. doi: 10.5194/essd-17-6647-2025.